ACS Photonics

Enhancing Complex Light Beam Propagation in Turbulent Atmosphere with Active Convolved Illumination

Anindya Ghoshroy, James Davis, Adrian A. Moazzam, Roohollah Askari, and Durdu Ö. Güney*

Cite This: *ACS Photonics* 2024, 11, 4541−4558

Read Online

ACCESS | Metrics & More | Article Recommendations | Supporting Information

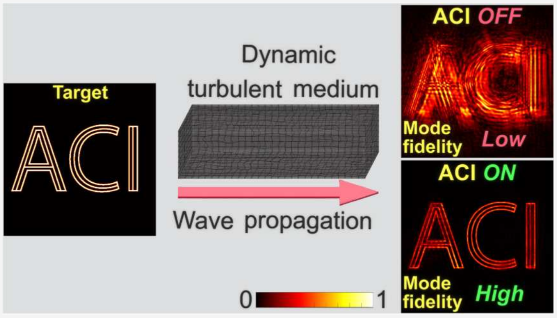

ABSTRACT: Robust transmission of spatial, spectral, or temporal distributions of light through complex disordered media such as a turbulent atmosphere, biological tissue, or turbid media remains a critical obstacle in many research fields involving imaging, diagnosis, sensing, and communications. Inspired from a virtual-gain technique for loss compensation in metamaterials, active convolved illumination (ACI) has been recently proposed as a ubiquitous optical compensation technique to significantly enhance information transport and hence data acquisition across lossy, noisy, or distorting media. The enhancement is achieved with an auxiliary source, which is correlated with the ground truth and ideally, when superimposed with the latter, perfectly compensates for any distortion incurred during the transmission process. In this work, we propose the first framework to implement ACI for robust coherent light transmission through a turbulent atmosphere. The auxiliary source is formulated from a reciprocal space characterization of the speckle pattern from a guide star or pilot beam. The proposed method can maintain high-fidelity wave propagation under moderately anisoplanatic conditions with an impressive 20-fold enhancement compared to the resolution limit of the turbulent atmosphere. We outline potential strategies to extend the framework to include dynamic turbulence and scattering effects. This work introduces a powerful tool for robust light transmission through disordered media and potentially can be seamlessly integrated with existing techniques and further extended to the broad spectrum of statistical sciences.

KEYWORDS: *turbulence, atmospheric propagation, anisoplanatism, distortion mitigation, orbital angular momentum beams, correlations, selective amplification*

■ INTRODUCTION

Rapid advances in high-resolution imaging technologies have enabled acquisition of detailed panoramic and three-dimensional images of complex samples with ultrahigh spatiotemporal precision.[1,2] Techniques such as structured illumination microscopy (SIM),[3] stimulated emission depletion (STED),[4,5] single-molecule localization microscopy (SMLM),[6−9] photoactivation localization microscopy (PALM),[8,10] and stochastic optical reconstruction microscopy (STORM)[11,12] have proven indispensable for biomedical imaging and diagnostic applications. In parallel, development of hybrid techniques such as correlative light-electron microscopy (CLEM)[13] has brought optical high resolution imaging close to the electron microscopy resolution.[14,15] However, robust light propagation in disordered or turbulent media remains a critical challenge in many fields such as deep-tissue imaging, optogenetics, free-space optical (FSO) communications, or remote sensing.[16] For example, in deep-tissue imaging, optically complex scattering and spatiotemporal refractive index inhomogeneities scramble wave propagation, resulting in higher order focal spot aberrations. This often restricts high-resolution visualization of samples.[17]

The topic of wave propagation in disordered media has evolved rapidly in recent years, fueled by advances in available technologies and computational methods. A plethora of new techniques[18,19] have been theoretically and experimentally demonstrated for diverse wave propagation regimes.[20,21] A straightforward approach utilizes the residual nonscattered or ballistic photons for image formation. Techniques such as confocal microscopy,[22] multiple-photon microscopy,[23−25] and optical coherence tomography[26] can reliably extract the nonscattered light for sharp image reconstruction at penetration depths beyond conventional microscopy. However, with increasing depth, the scattered field becomes overwhelmingly dominant restricting the achievable contrast and resolution solely from the nonscattered field.[27−29] Under such conditions, adaptive optics and wavefront shaping techni-

Received: April 15, 2024
Revised: October 1, 2024
Accepted: October 3, 2024
Published: October 15, 2024

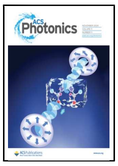

https://doi.org/10.1021/acsphotonics.4c00687

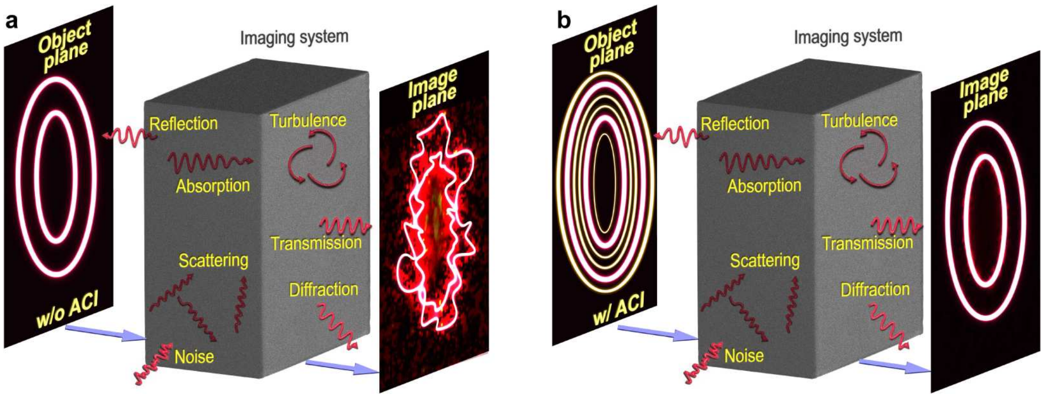

Figure 1. Operating principle of ACI for enhanced imaging. (a) Imaging systems, in general, are susceptible to information loss due to many optical processes including reflection, scattering, diffraction, absorption, noise, and turbulence, resulting in a low-fidelity image. (b) In ACI, the ground truth (pink concentric rings) is superimposed with a correlated auxiliary source (beige concentric rings), which is constructed using a spectral characterization of the underlying faulty channel. The auxiliary source then prevents information leakage from the system by compensating the adversary photons. The result is a remarkable data acquisition leading to a high-fidelity image.

ques[18,30] have been employed as effective alternatives. With adaptive optics, the low-order aberration effects from the scattered field can be effectively reversed under negligible absorption[19] and have demonstrated great success particularly in astronomical imaging. The distorted field is restored by first estimating the aberrated wavefront either computationally with iterative algorithms[31,32] or physically with wavefront sensors.[33] An equal and opposite tilt is applied using deformable mirror arrays or spatial light modulators (SLM) to the wavefront before or after propagation through the medium.[34,35] However, higher order aberration effects, strong scintillation, and branch points[36,37] affect the accuracy of estimating wavefront aberrations. Therefore, applications involving deep tissue imaging beyond 20 μm[38] or long distance propagation through a turbulent medium often require more sophisticated adaptable wavefront sensing or phase reconstruction algorithms to maintain robust, artifact-free wavefront correction.[36,39,40] However, inevitably higher order aberration effects become increasingly difficult if not practically impossible to accurately measure. This limits even moderately accurate correction of the scattered modes with wavefront sensing.[19] Under such circumstances, wavefront shaping offers a powerful alternative approach[18,30] since it is still possible to manipulate the distorted field within the memory effect of the medium.[41] The light field is modified with an SLM by first estimating the scattering matrix of the propagation either directly or with an iterative search.[42] A variety of wavefront shaping methods have been proposed, such as feedback-based,[43] optical phase conjugation,[44] transmission matrix measurement,[45] and deep-learning-based[46] wavefront shaping. Feedback-based wavefront shaping requires optimizing the wavefront with an SLM before propagation. A detector placed behind the scattering medium, photoaccoustics,[47,48] or implanted linear or nonlinear fluorescent guide stars[49−51] are some potential feedback sources. However, relatively long acquisition sequences and heavy computational burden[32] make them challenging for use in highly dynamic media due to limited acquisition speed or the field of view.[42,52] Optical phase conjugation fares better due to higher operational speed[53−55] but can sometimes exhibit relatively lower enhancement[55] and is hindered by the stringent requirement of a point source guide star.[19] Deep-learning and neural-network-based wavefront shaping methods are still in their infancy. However, they have great potential to improve the reconstruction fidelity while alleviating the requirements for exact modeling or estimating the medium's scattering matrix.

Although numerous techniques have been developed for different propagation regimes, their implementations are often restrictive or application-specific.[19] High performance can be maintained under specific propagation configurations or applications. For example, wavefront shaping techniques exhibit limited enhancement under long distance propagation through atmospheric turbulence, which is important in space optical communication or remote-sensing applications.[56] This is because most forms of structured light[57,58] have been theoretically and experimentally shown to be equally vulnerable to turbulence-induced distortions.[59] Additional constraints such as finite optical aperture sizes imply that phase conjugation cannot fully reverse the optical aberrations since information is partially lost during long distance transmission.[60] Consequently, distortion-resilient[61] or propagation-invariant forms of structured light[62,63] have been proposed as alternative solutions. Wave propagation in static disordered media generically supports formation and propagation of highly transmitting optical modes[30,63] through transmission eigenchannels.[64] Therefore, deploying such modes has been proposed for increasing FSO communication bandwidths.[16,65]

A major challenge that needs to be addressed is diversifying and furthering the operational bounds of current technologies. Here, we propose "active convolved illumination (ACI)" as a versatile technique for high-fidelity transmission of complex light beams through a turbulent atmosphere. The versatility of the ACI stems from the ubiquitous nature of its operating principle. This renders ACI amenable to integration with the existing methods and can potentially allow for the development of hybrid technologies with a superior performance.

The physical concept of ACI has been inspired from loss compensation in metamaterials with a type of virtual gain, where the adverse effect of absorption in the metamaterial has been compensated with an auxiliary source using a completely passive medium.[66,67] Since then, the original concept[66] has been extended to various types of system imperfections ranging from absorption and attenuation in near-field coherent and incoherent imaging[68−77] to shot noise in incoherent far-field imaging,[78] among others.[79] Promising results have been obtained in terms of enhancements in super- and diffraction-limited resolutions, spectral signal-to-noise ratio (SNR), image contrast, and tolerance to pixel saturation. However, none of those earlier works have considered the important problem of wave propagation in the presence of turbulence such as in atmospheric propagation or the imaging of biological tissues. Meanwhile, a different variant of virtual gain based on the complex frequency has also emerged and has been applied to enhanced super-resolution imaging.[80−82]

The operating principle of ACI is described in Figure 1 for faulty channels, taking an imaging system as an example. As illustrated in Figure 1a, imaging systems or any other faulty channels, in general, are prone to signal photon losses due to various optical processes including, for example, reflection, scattering, diffraction, absorption, noise, and turbulence. This impedes high-fidelity information transfer to the receiver plane from the object plane. It has been hypothesized that the loss of information arising from a wide variety of sources could be circumvented by ACI as depicted in Figure 1b.[78] In ACI, the ground truth (pink concentric rings) is superimposed with a correlated auxiliary source (red concentric rings). The auxiliary source regulates the object spectrum to mitigate the adversary photons and thus enables the transmission of the ground truth unscathed. The auxiliary source is prudently constructed using a spectral characterization of the faulty channel representing the reference system (Figure 1a).[77,78] In the ideal case of perfect transfer or reconstruction of the ground truth, the auxiliary source fully vanishes at the output.

The construction of the auxiliary source typically involves an optical convolution between the ground truth and a set of correlation-injecting sources (CISs). The CISs are designed based on the stochastic characteristics of the transmission channel. Through convolution, the CISs correlate the ground truth with the stochastic system and generate the auxiliary source superimposed on the ground truth. Therefore, the auxiliary source becomes correlated with both the ground truth and the stochastic system (i.e., the CISs inject correlations into the auxiliary source from both the stochastic system and the ground truth). In refs 75 and 83, hyperbolic metamaterials have been proposed to generate the CISs for near-field imaging. In ref 78, the CIS was generated by an increased exposure through an annular aperture in the pupil plane for far-field incoherent imaging. In the latter, the CIS was constructed using the fundamental principle that the spectral variance for shot noise is flat and proportional to the total expected power in the entire image. An important characteristic of the CISs in most of these previous works is that they form a finite set of orthogonal narrow-band beams that can selectively amplify[77,78,84] the object spectrum via optical convolution with high quality (e.g., enhanced spectral SNR).[77,78]

In this article, we develop a theoretical framework for enhancing wave propagation through turbulent media with the ACI technique for coherent light. This presents the first introduction of ACI to a turbulent medium and to its stochastic modeling — a significant step forward from previous ACI implementations.[72,74−79] Here, the auxiliary source is implemented using a combination of stochastic spectral phase correction (SPC) and selective amplification (SA).[77,78] The proposed framework is extensively tested with arbitrary field distributions under diverse propagation conditions. We show that high-fidelity wave propagation under moderately anisoplanatic conditions with an impressive 20-fold enhancement or more compared to the resolution limit of the system is achievable. We highlight multiple potential strategies that can further extend the framework into stronger and dynamic turbulence regimes. The results demonstrate the high versatility and ubiquity of ACI for distinct statistical problems with unique stochastic characteristics from noise mitigation in superlensing[74−77,83] to complex beam propagation through a turbulent atmosphere. Our findings foster new research in a broad range of disciplines, where statistical sciences play an important role, such as atmospheric sciences, seismology, imaging through turbulence, FSO communications, remote sensing, bioimaging, artificial intelligence, finance, and quantum information.

■ THEORY

In Supporting Information Section S1, we summarize the numerical model used throughout this work, which emulates wave propagation through a turbulent atmosphere. Below, we consider the essential mathematical properties of the ACI framework before presenting an implementation methodology for the system under consideration. Throughout this work, we consider waves propagating along the z-axis with transversal wavevector components k_x and k_y. Complex fields in physical and reciprocal space are related with a two-dimensional Fourier transform operator F as $U(k_x, k_y) = F\{u(x, y)\}$.

Consider a spatially coherent uniform plane wave normally incident on a planar transmissive or reflective target at the source plane, $z = 0$. The field distribution of the transmitted or reflected beam is denoted by $o(\mathbf{r}) \in C$ where $\mathbf{r} \in R^2$ denotes the position coordinate. The field of view (FOV) for $o(\mathbf{r})$ is assumed to be significantly smaller than the source plane dimensions. The instantaneous turbulence-distorted field distribution at the observation plane $z = L$ is $i_\mathrm{P}(\mathbf{r}) \in C$ and can be approximately related to $o(\mathbf{r})$ using a superposition integral as[85,86]

$$i_\mathrm{P}(\mathbf{r}_\mathrm{o}) = \iint o(\mathbf{r}_\mathrm{s}) s_\mathrm{t}(\mathbf{r}_\mathrm{o}, \mathbf{r}_\mathrm{s}) d^2\mathbf{r}_\mathrm{s} \tag{1}$$

where $(\mathbf{r}_s, \mathbf{r}_\mathrm{o}) \in R^2$ are the position coordinates of the source and observation planes, respectively, and $s_\mathrm{t}(\mathbf{r}_\mathrm{o}, \mathbf{r}_\mathrm{s})$ is a spatiotemporally varying point spread function (PSF). In this work, short-exposure imaging is assumed and the temporal evolution of $s_\mathrm{t}(\mathbf{r}_\mathrm{o}, \mathbf{r}_\mathrm{s})$ is discarded. Under isoplanatic conditions, eq 1 reduces to a convolution between $o(\mathbf{r}_\mathrm{s})$ and a shift-invariant PSF. For brevity, eq 1 is written using an operator notation as $i_\mathrm{P}(\mathbf{r}) = S_\mathrm{t}\{o(\mathbf{r})\}$. A correction technique can be used to estimate the ground truth from $i_\mathrm{P}(\mathbf{r})$ and is written in operator form as

$$\tilde{o}_\mathrm{P}(\mathbf{r}) = \mathcal{R}_\mathrm{P}\{i_\mathrm{P}(\mathbf{r})\} = \mathcal{R}_\mathrm{P}\{\mathcal{S}_\mathrm{t}\{o(\mathbf{r})\}\} \tag{2}$$

where $\tilde{o}_\mathrm{P}(\mathbf{r})$ is the reconstructed result and $\mathcal{R}_\mathrm{P}$ is a reconstruction operator. Potential candidates for $\mathcal{R}_\mathrm{P}$ include techniques such as traditional[87] or vectorial[88] adaptive optics, deep learning models,[89] blind deconvolution,[90,91] image registration methods,[92] or a hybrid combination of two or more methods.[93−98] For simplicity, we adopt $\mathcal{R}_\mathrm{P}$ as a basic deconvolution operator with a vacuum propagation PSF as the kernel. The PSF is calculated from the vacuum propagation of a point source using the angular spectrum method. In general, stochastic processes such as shot noise or electronic noise contribute to additional distortion in eq 1. The present work discards measurement noise partly because they were considered in past studies with ACI[74−77] but more importantly to emphasize on turbulence-induced distortions.

For long propagation paths or strong turbulence, $i_\mathrm{P}(\mathbf{r})$ acquires a complex intensity pattern due to a randomized multipath interference effect. This results in a poorly reconstructed version of the ground truth $\tilde{o}_\mathrm{P}(\mathbf{r})$. ACI's active optical compensation technique enhances the low-fidelity propagation step in eq 1 and consequently enables robust estimation of the ground truth with standard correction techniques. This enhancement is achieved with an auxiliary source, which is correlated with the ground truth and ideally, when superimposed with the latter, perfectly corrects any distortions $o(\mathbf{r})$ incurs during the transmission process. The ACI compensation technique is conceptualized in Figure 2.

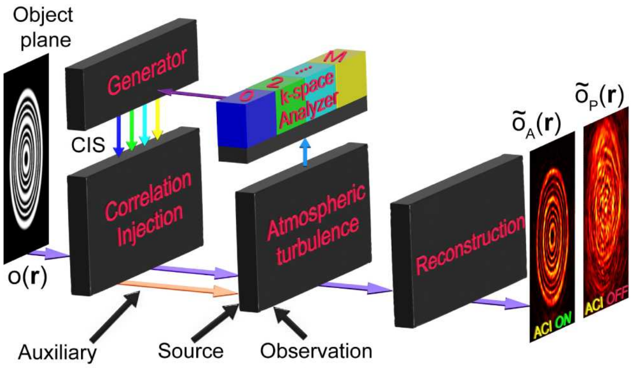

Figure 2. Conceptual schematic of the ACI technique. Turbulence-induced index fluctuations corrupt the fidelity of wave propagation and results in poor reconstruction of targets. In ACI, the ground truth (purple arrow) is superimposed with an auxiliary, which serves to compensate for the distortion that scrambles the ground truth as it traverses through the system. The auxiliary is correlated with the ground truth and is generated through convolution by injecting the ground truth with the CISs possessing the capability to correct distortions introduced by the system of concern. The CISs are typically formulated based on a reciprocal space distortion analysis. This results in a remarkably robust transmission of data through the distorting medium, and high reconstruction fidelity is feasible.

The auxiliary source can be generated by convolving $o(\mathbf{r})$ with an external source $c(\mathbf{r}) \in C$ referred to as the CIS. The CIS is strategically constructed by characterizing the reciprocal space behavior of the system's intrinsic stochastic processes. The CIS can be conceptualized as a beam containing the capability to correct distortions introduced by the system under consideration. Through convolution, this unique property can be injected into an arbitrary beam with an unknown spatial field distribution. The resulting modified source $o_\mathrm{A}(\mathbf{r})$ is called the correlation-injected source and is expressed as

$$o_\mathrm{A}(\mathbf{r}) = o(\mathbf{r})*c(\mathbf{r}) = \sum_{j=0}^{M} o(\mathbf{r})*c_j(\mathbf{r}) = \sum_{j=0}^{M} o_{j,\mathrm{A}}(\mathbf{r}) \tag{3}$$

where * denotes convolution. $c_j(\mathbf{r})$ is the jth CIS and $o_{j,\mathrm{A}}(\mathbf{r})$ is the corresponding correlation-injected source. The auxiliary source is defined as the modification introduced to $o(\mathbf{r})$, and it is superimposed with the latter in eq 3 as a single undivided injected source. Alternatively, the injected source can also be written as $o_\mathrm{A}(\mathbf{r}) = o(\mathbf{r}) + a(\mathbf{r})$, where $a(\mathbf{r})$ is the auxiliary source correlated with both $o(\mathbf{r})$ and $c(\mathbf{r})$. The auxiliary source is spatially and temporally coherent with respect to $o(\mathbf{r})$. We analyzed the potential impact of spatially and temporally quasicoherent sources on the performance of ACI in Section S3, which suggests that ACI retains high-fidelity wave propagation through turbulence for quasi-coherent sources.

The jth CIS in eq 3 is developed by analyzing the stochastic behavior of a portion of the total reciprocal space bandwidth of the system. Therefore, each $c_j(\mathbf{r})$ in Eq 3 can provide distortion mitigation for a controlled band of spatial frequencies. Using $M + 1$ unique CISs, this mitigation can be provided sequentially to the entire reciprocal space bandwidth of the system under consideration. Introduction of a CIS implies that additional energy is being provided to the system. The word "active" is used to distinguish this and should not be confused with active optical gain. Additionally, the CIS is not a propagation-invariant solution of the Helmholtz equation.[99] The hypothesized distortion mitigation behavior should not be confused with eigenmodes[62] or self-healing beams.[100] In this work, the auxiliary source is implemented using a combination of stochastic spectral phase correction and the previously employed[77,78] selective amplification method.

Consider a coherent beam whose reciprocal space spectrum can be defined as a band-limited function as

$$V(\mathbf{k}) = V_0 \exp\left\{-\frac{(k-k_\mathrm{c})^n}{W^n}\right\} \times \exp\{il\phi\} \tag{4}$$

where $k^2 = |k_x|^2 + |k_y|^2$ and k_x and k_y are the components of the transverse wavevector $\mathbf{k} \in R^2$. The first exponential term is a super-Gaussian annular function, where $n = 6$ is used throughout this work. V_0, $k_\mathrm{c}^2 = |k_{\mathrm{c},x}|^2 + |k_{\mathrm{c},y}|^2$, and W control the peak amplitude, the radial center frequency, and width, respectively, of the super-Gaussian annulus. The parameter $l \in I$ and controls the helicity of a vortex phase where $\phi = \tan^{-1}(k_y/k_x)$. Therefore, $v(\mathbf{r}) = F^{-1}\{V(\mathbf{k})\}$ is a beam carrying orbital angular momentum (OAM) with a topological charge l. In principle, the functional form of $v(\mathbf{r})$ can be substituted with other OAM modes such as the Laguerre−Gaussian or Bessel beams as long as the reciprocal space profile exhibits properties similar to eq 4. We choose to work with eq 4 partly for mathematical and illustration convenience but more importantly to allow precise control of the spectrum $V(\mathbf{k})$. Let us consider a stack of $M + 1$ such OAM modes, where the jth mode is denoted as $v_j(\mathbf{r}) = F^{-1}\{V_j(\mathbf{k})\}$ and $V_j(\mathbf{k})$ follows eq 4 with unique $V_{0,j}$, $k_{\mathrm{c},j}$, W_j, and l_j.

The proposed ACI framework is conceptualized in Figure 3 and is split into four stages for pedagogical purposes. The SPC method includes the first three stages and is illustrated in Figure 3a, and the SA method is illustrated in Figure 3b. Example spatial intensity distributions of the OAM modes are shown in Figure 3a. In the first stage (see Figure 3a), the stack of $M + 1$ OAM modes is propagated sequentially through a turbulent atmosphere assumed to be frozen in time. The resulting complex field distribution at the observation plane for the jth OAM mode can be described according to eq 1 as $i_{v_j,\mathrm{P}}(\mathbf{r}) = S_\mathrm{t}\{v_j(\mathbf{r})\}$. In the second stage of the framework, $i_{v_j,\mathrm{P}}(\mathbf{r})$ is used for the reconstruction, according to eq 2, that is,

$$\tilde{v}_{j,\mathrm{P}}(\mathbf{r}) = \mathcal{R}_\mathrm{P}\{i_{v_j,\mathrm{P}}(\mathbf{r})\} = \mathcal{R}_\mathrm{P}\{\mathcal{S}_\mathrm{t}\{v_j(\mathbf{r})\}\} \tag{5}$$

where $\tilde{v}_{j,\mathrm{P}}(\mathbf{r})$ is the distorted version of $v_j(\mathbf{r})$ and is illustrated in Figure 3a. The spatial geometric distortion in $\tilde{v}_{j,\mathrm{P}}(\mathbf{r})$ will approximately manifest as a phase perturbation distributed over reciprocal space. The perturbations within the bandwidth

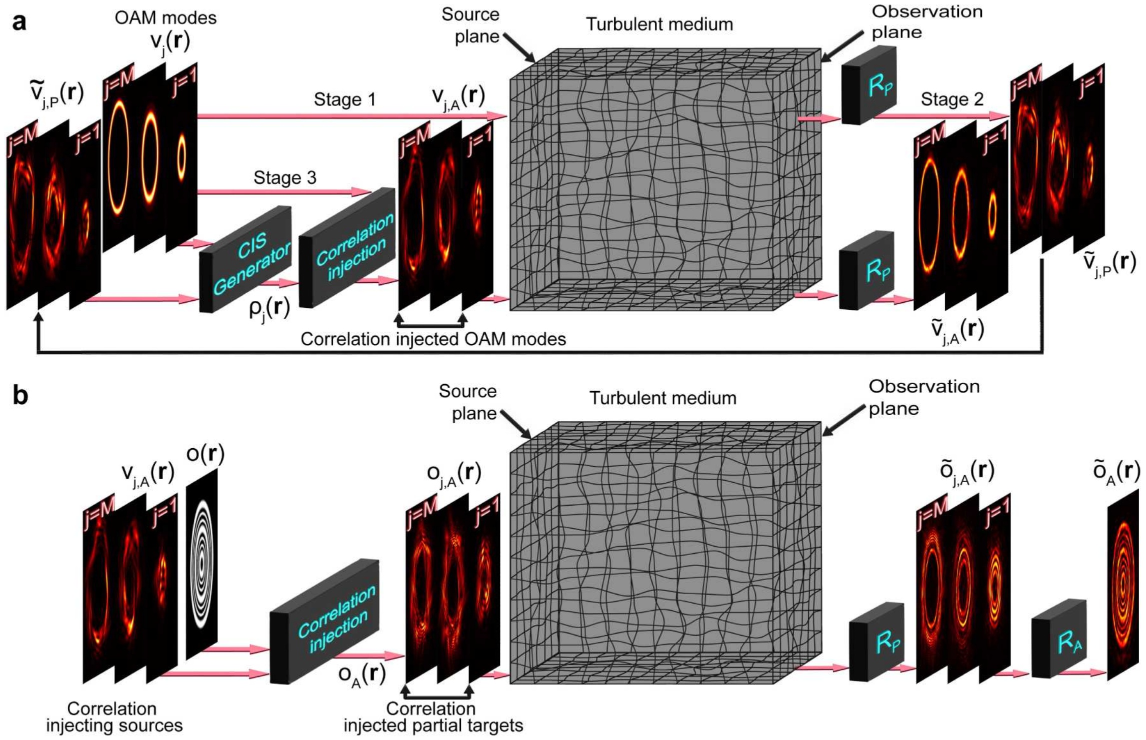

Figure 3. ACI framework for wave propagation through turbulent media is decomposed into four stages. (a) Spectral phase correction comprises the first three stages. A sequence of OAM modes with different reciprocal space parameters is sequentially propagated through the medium. The jth mode is used to characterize the instantaneous spectral distortion within the controllable bandwidth $k_{c,j} - W_j \leq k \leq k_{c,j} + W_j$. For $j = 0$ (not depicted), $0 \leq k \leq W_0$. A CIS is generated that contains the conjugate of the estimated distortion for the corresponding bandwidth. Through convolution, each CIS is injected into the corresponding OAM mode, and the injected mode is propagated through the same realization of the turbulent medium. The observed enhancement can be maximized by adjusting the parameters $V_{0,j}$, $k_{c,j}$, W_j, and l_j of each OAM mode. (b) In the selective amplification process, the optimized stack of $M + 1$ correlation-injected OAM modes is deployed as the CISs for an arbitrary target $o(\mathbf{r})$. This decomposes the ground truth into a stack of correlation-injected partial targets, which are propagated sequentially through the same realization of the turbulent medium. The CISs enable each partial target to propagate in a minimally distorted state.

$2W_j$ (W_0 for $j = 0$) are extracted. A new beam $\rho_j(\mathbf{r})$ is generated, which is defined in reciprocal space as

$$\rho_j(\mathbf{k}) = \rho_{0,j}(\mathbf{k})\exp\{i[\phi_{V_j}(\mathbf{k}) - \phi_{\tilde{V}_j}(\mathbf{k})]\} \tag{6}$$

where $\phi_{Vj}(\mathbf{k})$ and $\phi_{\tilde{V}j}(\mathbf{k})$ are the phases of $V_j(\mathbf{k})$ and $\tilde{V}_{j,P}(\mathbf{k})$, respectively. We assume $\rho_{0,j}(\mathbf{k}) = 1$ throughout this work. In physical space $\rho_j(\mathbf{r}) = F^{-1}\{\rho_j(\mathbf{k})\}$ is designated as the CIS for the jth OAM mode and a similar process is repeated for all $M + 1$ modes. In the third stage (see Figure 3a), each CIS beam is convolved with the corresponding $v_j(\mathbf{r})$ to obtain the correlation injected OAM mode $v_{j,A}(\mathbf{r})$ expressed as

$$v_{j,A}(\mathbf{r}) = v_j(\mathbf{r})*\rho_j(\mathbf{r}) \tag{7}$$

The injected OAM modes are propagated through the same realization of the turbulent atmosphere. The resulting complex field on the observation plane is reconstructed similar to eq 5 and is written as

$$\tilde{v}_{j,A}(\mathbf{r}) = \mathcal{R}_P\{\mathcal{S}_t\{v_j(\mathbf{r})*\rho_j(\mathbf{r})\}\} \tag{8}$$

where $\tilde{v}_{j,A}(\mathbf{r})$ is the reconstructed OAM mode with ACI. Figure 3a illustrates a comparison between $\tilde{v}_{j,A}(\mathbf{r})$ and $\tilde{v}_{j,P}(\mathbf{r})$. In subsequent discussions, eqs 5 and 8 are used to optimize the performance of the CIS beam in Eq 6. The above technique is referred to as SPC.

We should mention that Figure 3 is more representative of an FSO communication link with access to both sides of the channel, and it assumes a tabletop-like setup. Therefore, the OAM beam is located on the source side of Figure 3a. Different application-specific probe configurations are discussed in refs 19 and 101 where access to the distal side may or may not be available. Employing the reciprocity of the medium[102] and initiating the OAM beam rather from the receiver side as a guide star or pilot beam,[101] $\tilde{v}_{j,P}(\mathbf{r})$ can also be directly obtained at the transmitter side. Note that the main goal here is not the transmission of the OAM beams but the unknown complex targets (e.g., unknown to the receiver in an FSO communication link), as illustrated in Figure 3b.

We now consider a few important assertions about the generated CIS beam and its overall role in the SPC method. First, the right-hand side of eq 6 represents an example reciprocal space characterization of the spatiotemporal snapshot of the conjugate of the turbulence induced distortion at the moment $v_j(\mathbf{r})$ propagated through the medium. Second, the band limited form of $V(\mathbf{k})$ in eq 4 is intended to limit the characterization to the spatial frequency bandwidth $2W_j$ (W_0 for $j = 0$). Third, assuming perfect characterization is achievable with eq 6, then the CIS $\rho_j(\mathbf{r})$ is essentially a beam that can perfectly correct the aberrations it would experience within the same bandwidth. Finally, the convolution in eq 7 implies that the above property is injected into the OAM beam $v_j(\mathbf{r})$. Therefore, as $v_{j,A}(\mathbf{r})$ propagates through the medium, the contribution of CIS is entirely absorbed and the resulting diffraction pattern on the observation plane is expected to have fewer residual aberrations since the bandwidth of $\nu_j(\mathbf{r})$ overlaps well with $\rho_j(\mathbf{r})$.

In the final step of the ACI framework, the SPC method is integrated with SA. This is illustrated in Figure 3b. Assume that $o(\mathbf{r})$ has an unknown power spectral density profile confined within the Nyquist bandwidth. Let the $M + 1$ OAM modes be designed in such a way (by controlling $k_{c,j}$ and W_j) that their superposition spans all spatial frequencies within the Nyquist bandwidth. The jth correlation injected OAM mode $\nu_{j,A}(\mathbf{r})$ is now used as the new CIS (see Figure 3b) to obtain the jth correlation injected partial target, which can be expressed by modifying eq 7 as $o_{j,A}(\mathbf{r}) = o(\mathbf{r}) * \nu_{j,A}(\mathbf{r})$. Therefore, total injected target is written as superposition of $o_{j,A}(\mathbf{r})$ as

$$\begin{aligned} o_{A}(\mathbf{r}) &= \sum_{j=0}^{M} o_{j,A}(\mathbf{r}) = \sum_{j=0}^{M} o(\mathbf{r}) * \nu_{j,A}(\mathbf{r}) \\ &= \sum_{j=0}^{M} o(\mathbf{r}) * \nu_j(\mathbf{r}) * \rho_j(\mathbf{r}). \end{aligned} \tag{9}$$

Therefore, each injected partial target in eq 9 is a selectively amplified spectral segment of the original target with bandwidth $2W_j$ (W_0 for $j = 0$). Furthermore, each segment is injected with the estimated conjugate of the turbulence-induced aberration. The convolution term in eq 9 represents the combination of SA with SPC since the amplitude of the target spectrum is selectively amplified by the factor $V_{0,j}$ within $2W_j$ (W_0 for $j = 0$). Note that the super-Gaussian profile of $|V_j(\mathbf{k})|$ in eq 4 provides an approximately uniform amplification within the bandwidth $2W_j$ (W_0 for $j = 0$).

The stack of $M + 1$ injected partial targets in eq 9 is propagated through the turbulent medium sequentially. The ground truth is reconstructed with the following steps. First, the complex fields on observation plane are deconvolved with the vacuum propagation PSF. The reconstructed jth injected partial target is denoted by $\tilde{o}_{j,A}(\mathbf{r})$ and is expressed as

$$\tilde{o}_{j,\mathrm{A}}(\mathbf{r}) = \mathcal{R}_{\mathrm{P}}\{\mathcal{S}_{\mathrm{t}}\{o(\mathbf{r}) * \nu_j(\mathbf{r}) * \rho_j(\mathbf{r})\}\} \tag{10}$$

An ACI convolution operator is then defined for each $\tilde{o}_{j,\mathrm{A}}(\mathbf{r})$, which is denoted by $\mathcal{R}_{j,\mathrm{A}}$. The kernel of $\mathcal{R}_{j,\mathrm{A}}$ is expressed in reciprocal space as

$$R_{0,\mathrm{A}}(\mathbf{k}) = \frac{1}{1 + V_{j=0}(\mathbf{k})} \exp\left\{\frac{-k^4}{2\mathcal{W}_1^4}\right\} \tag{11}$$

for the $j = 0$ mode and

$$R_{j,\mathrm{A}}(\mathbf{k}) = \frac{\sum_{\alpha=1}^{\beta} \exp\{-[k - k_j(\alpha)]^2 / 2\mathcal{W}_2^2\}}{1 + V_j(\mathbf{k})} \tag{12}$$

for all $1 \leq j \leq M$ where

$$k_j(\alpha) = k_{\mathrm{c},j} + 1.51\alpha\mathcal{W}_2 \tag{13}$$

$R_{0,\mathrm{A}}(\mathbf{k})$ and $R_{j,\mathrm{A}}(\mathbf{k})$ are essentially two window functions specifically designed for the functional form of the OAM modes in eq 4 to restore the power spectral density profile of arbitrary targets. The parameters $\mathcal{W}_1$, $\mathcal{W}_2$, and β are used to control the reciprocal space width of each window function and will be detailed in subsequent discussions. Finally, the ground truth is restored by first deconvolving $\tilde{o}_{j,\mathrm{A}}(\mathbf{r})$ with the corresponding ACI reconstruction operator and superimposing the results. This step can be expressed as

$$\begin{aligned} \tilde{o}_{\mathrm{A}}(\mathbf{r}) &= \sum_{j=0}^{M} \mathcal{R}_{j,\mathrm{A}}\{\tilde{o}_{j,\mathrm{A}}(\mathbf{r})\} \\ &= \sum_{j=0}^{M} \mathcal{R}_{j,\mathrm{A}}\{\mathcal{R}_{\mathrm{P}}\{\mathcal{S}_{\mathrm{t}}\{o(\mathbf{r}) * \nu_j(\mathbf{r}) * \rho_j(\mathbf{r})\}\}\}. \end{aligned} \tag{14}$$

An illustrative example of this reconstruction step is shown in Figure 3b. Note that eq 14 is similar to the methods used in previous studies on ACI.[77,78] Finally, it should be noted that the passive reconstruction step in eq 10 can be substituted with more sophisticated reconstruction methods such as adaptive optics, deep learning, or blind deconvolution.[87−91]

We conclude this section by briefly presenting the figure of merit metrics used in subsequent analyses to objectively quantify and differentiate wave propagation performance with and without ACI. First, let $u(\mathbf{r})$ and $\tilde{u}(\mathbf{r})$ be the complex fields at the source plane and the corresponding reconstructed result, respectively. The spatial normalized cross-correlation (NCC) between $|u(\mathbf{r})|^2$ and $|\tilde{u}(\mathbf{r})|^2$ for zero displacement is expressed as $\xi = |u(\mathbf{r})|^2 \star |\tilde{u}(\mathbf{r})|^2$ and $\star$ denotes cross-correlation. All of the reconstructions involve both the phase and amplitude, but the phase of the final reconstructions is discarded leaving us with only intensity (or amplitude). Because we are interested only in propagating the intensity distribution with a minimal distortion, therefore, ξ is used to compare the state of distortion in the reconstructed result and can be used to assess the impact of turbulence.[56] The NCC results for wave propagation with and without ACI are denoted as ξ_{A} and ξ_{P}, respectively. Second, the severity of turbulence is generally quantified with D/r_0, where D is an imaging aperture at the observation plane and r_0 is the Fried parameter. This ratio imposes two limiting cases. When $D/r_0 < 1$, the resolution of the system is limited by its aperture, and when $D/r_0 < 1$, the atmosphere limits the systems ability to resolve an object. In this work, the original definition of D/r_0 is adjusted without loss of generality to broaden the scope of results. We define D as the diameter of a phantom circular aperture enclosing $1 - 1/e^2$ of the total power contained within the diffraction pattern of $u(\mathbf{r})$ at the observation plane after vacuum propagation. The angular resolution of this aperture on the source plane is $1.22\lambda/D$ and the corresponding spatial resolution is $\Delta l_{\mathrm{s}} = 1.22L\lambda/D$, where λ is the wavelength. The Fried parameter (r_0) represents an equivalent radius of a diffraction-limited circular aperture subject to degradation by turbulence over long exposures. Therefore, the atmospheric spatial resolution limit can be written as $\Delta l_{\mathrm{t}} = 1.22L\lambda/r_0$. If $u(\mathbf{r})$ contains spatial features separated by less than Δl_{t}, then $\tilde{u}(\mathbf{r})$ will be obscured by the fine structure of a speckle pattern for short exposures and blurred by the seeing disk in long exposures. The ratio $\Delta l_{\mathrm{t}}/\Delta l_{\mathrm{s}}$ can be used to assess the expected severity of turbulence-induced aberrations. This first enables the analysis of arbitrary beams with diverse spatial profiles under variable propagation conditions. Second, since $\Delta l_{\mathrm{t}}/\Delta l_{\mathrm{s}}$ preserves the same interpretation as the conventional D/r_0, it serves as a useful alternative for communicating equivalency in the presented results with diverse imaging or wave propagation applications.

RESULTS

We now examine the wave propagation behavior under the ACI framework for different turbulent conditions within $2.5 \times 10^{-15} \leq C_n^2 \leq 3.5 \times 10^{-14}$ m$^{-2/3}$, where C_n^2 is the refractive index structure parameter. We assume the propagation distance is $L = 1$ km, and the wavelength is $\lambda = 1550$ nm. Using NCC calculations, we assess the state of distortion in the reconstructed results and evaluate the capability to propagate the original spatial distribution in a minimally distorted state. The SPC method is considered first. Wave propagation of OAM modes is simulated using the split-step process with and without ACI (see Section S1). The corresponding reconstructed results $|\tilde{\nu}_{j,\mathrm{A}}(\mathbf{r})|^2$ and $|\tilde{\nu}_{j,\mathrm{P}}(\mathbf{r})|^2$ are compared with the ground truth. Second, an optimization approach is proposed to maximize the observable enhancement. Third, we study the integration of SPC and SA methods. The reconstructed results for an arbitrary field distribution are compared with and without ACI. Lastly, we probe the limits of the overall framework by simulating wave propagation of multiple targets with varying spatial sophistication with and without ACI under increasingly severe turbulent conditions. Throughout the analyses, we study the behavior of the auxiliary and CIS under the selected propagation conditions.

Spectral Phase Correction and Correlation Injection Optimization. We first simulate propagation of three arbitrarily selected OAM modes through turbulence with and without ACI. The OAM mode structure is controlled by adjusting the reciprocal space parameters V_0, k_c, W, and l in eq 4. We initially consider a turbulence strength of $C_n^2 = 0.5 \times 10^{-14}$ m$^{-2/3}$. The corresponding Fried parameter is $r_0 = 21.42$ cm and the resolution limit is $\Delta l_t = 0.88$ cm. The isoplanatic patch and Rytov variance are $\theta_t = 6.73$ cm and $\sigma_\chi^2 = 0.01$, respectively. The reconstructed results $\tilde{\nu}_\mathrm{P}(\mathbf{r})$ and $\tilde{\nu}_\mathrm{A}(\mathbf{r})$ are obtained with eqs 5 and 8, respectively. The NCC results $\xi_\mathrm{A} = |\nu(\mathbf{r})|^2 \star |\tilde{\nu}_\mathrm{A}(\mathbf{r})|^2$ and $\xi_\mathrm{P} = |\nu(\mathbf{r})|^2 \star |\tilde{\nu}_\mathrm{P}(\mathbf{r})|^2$ are used to assess the fidelity of wave propagation with and without ACI. The results of the analysis are presented in Figure 4 where each subfigure shows the normalized spatial intensity distribution over a 4 × 4 cm^2 area. The OAM mode parameters are detailed in Figure 4a. Note that $V_0 = 1$ Am and $W = 43$ m^{-1} are used for this calculation.

The passively reconstructed results are shown in Figure 4b. Since the width of each annulus in Figure 4a is considerably smaller than Δl_t, the reconstructed mode structure in Figure 4b exhibits severe geometric distortion. Tip-tilt and higher order aberration effects are noticeable. The mode centroid is noticeably shifted from the optical axis (blue cross), and the annular profile is disrupted by a speckle pattern. This results in poor ξ_P. For longer propagation distances through volumetric turbulence, the distortion effects are significantly severe. The impact, for example, in free-space communication links[103,104] is often significant enough to restrict classical and quantum communication channels with structured light to only a few hundred meters.[97] Using ACI's proposed SPC method, the estimated CIS is generated based on eq 6. The CIS is injected into the OAM mode according to eq 7. The resulting correlation-injected OAM modes are shown in Figure 4c. Each injected mode after propagation through the atmosphere is reconstructed to obtain the result shown in Figure 4d where strong suppression of both tip-tilt and higher-order aberration effects is evident. The reconstructed annular mode profile has good contrast with minimal residual distortions, and a high ξ_A is obtained.

It is instructive to point out the potential advantages of ACI's reciprocal space distortion characterization and subsequent injection into the OAM mode. Generally, the higher-order aberration effects visible in Figure 4b would be distributed throughout the reciprocal space. Therefore, within the bandwidth of the OAM beam, the distortion and the corresponding correction can be potentially estimated with greater accuracy than conventional physical space methods.[18,19,34,35] Similarly, the estimated correction would also potentially exhibit higher tolerance to stronger higher order aberration effects and branch points with increasing C_n^2 due to the continual redistribution over the entire reciprocal space. By correlating the OAM mode to the CIS via convolution, distortion mitigation is potentially achievable with a minimal change to the subsequent reconstruction technique. Therefore, the ACI framework is suitable for integration with other techniques, such as adaptive optics or wavefront shaping. In principle, this would potentially enable the hybrid technique to operate in regimes beyond which robust independent operation of either is feasible. The estimation of the CIS and the injection process in eqs 6 and 7, respectively, particularly under stronger anisoplanatic conditions is a critical challenge. Note that in the present framework, the convolution between $\nu(\mathbf{r})$ and $\rho_j(\mathbf{r})$ in Eq 7 implies that the same SPC is injected throughout the spatial profile of $\nu(\mathbf{r})$. However, as the angular size of $\nu(\mathbf{r})$ increases relative to the isoplanatic angle θ_0, stronger anisoplanatism would necessitate multiple different profiles for $\rho_j(\mathbf{r})$. The tolerance of present method to anisoplanatism is considered in the subsequent discussion where the above study is repeated by increasing C_n^2 incrementally up to four times.

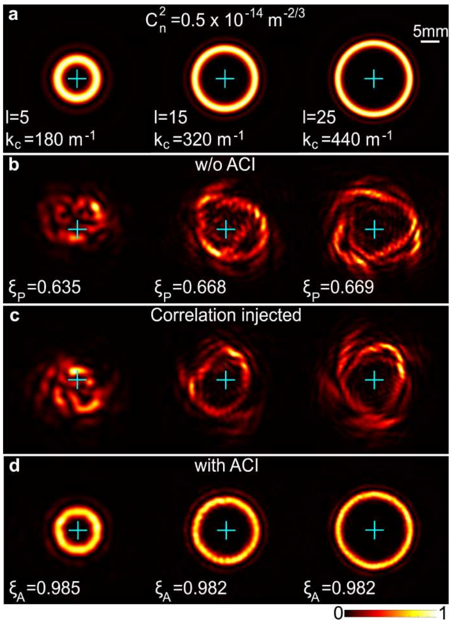

Figure 4. Implementation of the SPC method with OAM modes. Normalized intensity distributions of (a) three OAM modes and (b) their reconstructed results after propagation through turbulence without ACI. The CIS for each mode is calculated from the complex field versions of panels a and b and is injected into the corresponding OAM mode to obtain (c) the correlation injected mode (normalized intensity is shown). This is propagated through the same realization of turbulence. The reconstructed results are shown in panel d. Tip-tilt and higher order aberrations have disrupted the annular mode profile of the mode in panel b, yielding a poor ξ_P. The active result is reconstructed with minimal residual aberrations to the annular mode profile, thereby yielding a high ξ_A exceeding 0.98.

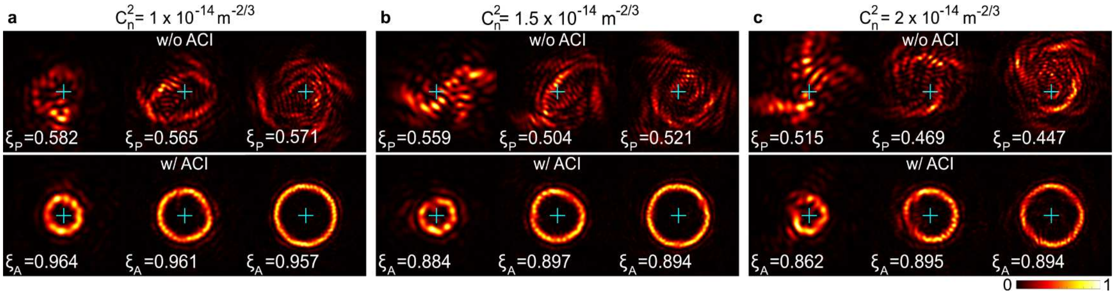

Figure 5. SPC method evaluated with increasing C_n^2 to study the cumulative impact of higher order aberrations under anisoplanatic conditions. The selected OAM modes profiles are shown in Figure 4a. Normalized intensity distributions plotted over a 4 × 4 cm^2 area for the reconstructed OAM modes without and with ACI are shown in the first and second rows, respectively for (a) $C_n^2 = 1 \times 10^{-14}$ m$^{-2/3}$, (b) $C_n^2 = 1.5 \times 10^{-14}$ m$^{-2/3}$, and (c) $C_n^2 = 2 \times 10^{-14}$ m$^{-2/3}$. Tip-tilt and higher order aberrations are significantly stronger with increasing C_n^2. Consequently, the annular mode profile is unrecognizable in the first rows of panels a, b, and c. In contrast, wave propagation with ACI maintains a reasonably strong enhancement. The residual distortions can be attributed to the loss of accuracy of the estimated CIS due to anisoplanatism.

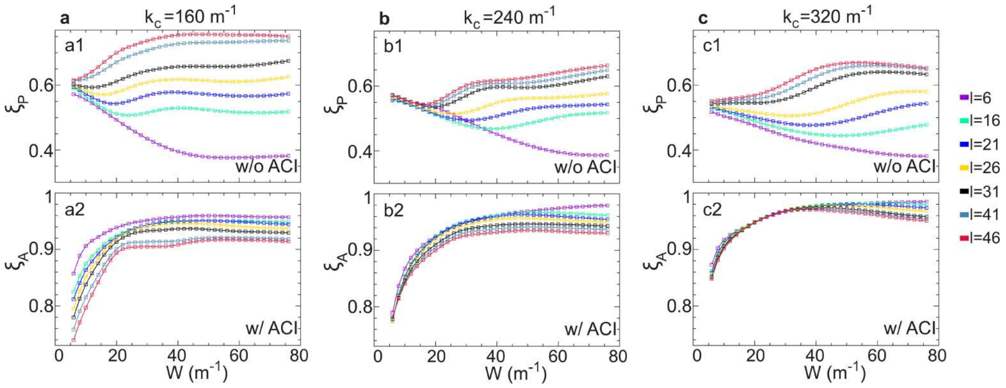

Figure 6. Optimization of the reciprocal space parameters of the OAM mode illustrated for (a) k_c = 160 m^{-1}, (b) k_c = 240 m^{-1}, and (c) k_c = 320 m^{-1}. The NCC results ξ_P and ξ_A are plotted as a function of W for the selected values of l. The overall goal is to obtain a set of mode parameters to maximize the observable ξ_A values for all spatial frequencies. From a2, b2, and c2, at approximately W = 40 m^{-1}, a high ξ_A was observed for a broad range of spatial frequencies. Interestingly, a1, b1, and c1 show a small improvement in ξ_P with increasing l. However, this behavior is reversed in a2, b2, and c2, which suggests that the increasing helicity of the OAM mode phase profile could be adversely affecting the SPC method.

The considered C_n^2 values are 1 × 10^{-14}, 1.5 × 10^{-14}, and 2 × 10^{-14} m$^{-2/3}$. This degrades the resolution limit to Δl_t = 1.33, 1.71, and 2.03 cm, respectively, and strengthens anisoplanatism by reducing the isoplanatic patch to θ_t = 4.441, 3.482, and 2.929 cm, respectively. The OAM modes in Figure 4a are reused in this study. The results are listed in Figure 5. The normalized spatial intensity distributions of the active and passive reconstructed results and their NCC results ξ_A and ξ_P are shown in the first and second rows for the corresponding C_n^2. Tip-tilt and higher-order aberrations in the passive reconstructed results are noticeably stronger than those in Figure 4b and increasingly distorted from Figures 5a−c to the point where the original OAM mode structure is completely obliterated. Consequently, ξ_P is poorer than that in Figure 4b and drops to below 0.5 in Figure 5c for the second and third modes. Remarkably, the active reconstruction maintains reasonably strong enhancement. The annular mode profile has good contrast, although small distortions are visible in the second row in Figure 5. Note that a less prominent outer concentric ring (see Figure 4a) that was clearly distinguishable in Figure 4d is now visibly worse in each case in the second row of Figure 5, eventually becoming indistinguishable in Figure 5c. This is attributed to the increased anisoplanatism and the resulting reduction in the effectiveness of the CIS.

An optimization of the reciprocal space parameters V_0, k_c, W, and l of the OAM mode in eq 4 is done to maximize ξ_A for all spatial frequencies within the Nyquist bandwidth. For an arbitrary k_c, a parametric sweep over W within the range $6 \leq W \leq 76$ m^{-1} is simulated for a constant l. The process is repeated by incrementing l to cover the range $1 \leq l \leq 80$. The beam parameters for $l = 0$ are determined last. The OAM mode corresponding to each set of parameters is propagated through turbulence with and without ACI. ξ_A and ξ_P are calculated from the active and passive reconstructed results, respectively. Optimization was performed for $C_n^2 = 1.5 \times 10^{-14}$ m$^{-2/3}$ and the results for k_c = 160, 240, and 320 m^{-1} are plotted in Figure 6a−c, respectively. For each k_c, the corresponding NCC result ξ_P is plotted as a function of W for various l values in Figure 6a1−c1. The corresponding active versions are shown in Figure 6a2−c2, respectively. Based on Figure 6a2−c2, for approximately W = 40 m^{-1}, ξ_A was observed to be high for all spatial frequencies. Therefore, W = 43 m^{-1} was adopted as the common width. The finalized optimized parameters are presented in Table 1. We point out that the optimization can be further improved by assuming the variable W. However, for simplicity in the reconstruction process, a constant value is adopted. Based on Figure 6a1−c1, we find that the selected OAM mode performs better with increasing l. Interestingly, this behavior is not maintained with ACI as seen in Figure

Table 1. Optimized OAM Beam Parameters for $V_j(\mathbf{k})$

j	V_0 (Am)	W (m^{-1})	k_c (m^{-1})	l
0	1	45	0	0
1	5	43	80	8
2	5	43	160	15
3	15	43	240	21
4	15	43	320	31
5	15	43	400	40
6	35	43	480	46
7	35	43	560	54
8	35	43	640	65
9	35	43	720	70

6a2−c2. This could suggest that the performance of SPC might be affected by the increasing helicity of the OAM beam. The observable enhancement in ξ_A over ξ_P will therefore be maximum over a range of l values before decaying. It is important to note that the observed behavior of the OAM mode with and without ACI in Figure 6 is unique to the definition of $v(\mathbf{r})$. Since the selected mode is adopted for a proof of concept illustration, the optimization process is left to future works with other more commonly studied OAM modes such as Laguerre−Gaussian, Bessel, Hermite−Gaussian, and Ince−Gaussian modes. We conclude this discussion by mentioning that each of the OAM modes in Table 1 is designed to implement SPC and SA within an 80 m^{-1} bandwidth. An overlap of 3 m^{-1} between adjacent modes is intended to minimize reconstruction artifacts with eq 14.

ACI Performance with Arbitrary Targets. We now investigate the performance of the ACI framework in the context of propagating arbitrary beams with diverse geometric patterns and complexities. The CIS $\rho_j(\mathbf{r})$ for the jth OAM mode is first calculated according to eq 6. An arbitrary target is decomposed into a stack of ten correlation injected partial targets according to eq 9. Wave propagation of the jth correlation injected partial target is simulated to obtain the complex field distribution on the observation plane. The reconstructed result is calculated with eq 14 to obtain $\tilde{o}_A(\mathbf{r})$. The convolution kernel for $\mathcal{R}_{j,A}$ was optimized using a radially symmetric calibration target with a power spectral density spanning the entire Nyquist bandwidth. For the major part of this work, we consider wave propagation of radially symmetric spatial field distributions to minimize the reconstruction artifacts. For $j = 0$, $\mathcal{W}_1 = 35$ m^{-1} is used in eq 11, and for $1 \leq j \leq 9$, $\beta = 13$ and $\mathcal{W}_2 = 4$ m^{-1} are used in eq 12. Note that the parametrization of eqs 11 and 12 is tied to the reciprocal space mode profile of the OAM beam and should be adjusted accordingly for different OAM beams. The target is also propagated without ACI, and the corresponding reconstructed result is obtained from eq 2 to yield $\tilde{o}_P(\mathbf{r})$. We continue to use the NCC results $\xi_A = |o(\mathbf{r})|^2 \star |\tilde{o}_A(\mathbf{r})|^2$ and $\xi_P = |o(\mathbf{r})|^2 \star |\tilde{o}_P(\mathbf{r})|^2$ to differentiate the fidelity of wave propagation with and without ACI, respectively. Additionally, we incorporate $\Delta l_t/\Delta l_s$ and the anisoplanatism factor θ_s/θ_t (Section S1) to quantify the expected severity of turbulence-induced distortions for the selected wave propagation conditions. We consider a turbulence strength of $C_n^2 = 1.5 \times 10^{-14}$ m$^{-2/3}$ for which Δl_t =1.71 cm, $\sigma_\chi^2 = 0.03$, and θ_t = 3.482 cm, respectively.

The results of this study are presented in Figure 7. Normalized intensity distributions are plotted over a 6 × 6 cm^2 area in Figure 7a−c and over a 9 × 9 cm^2 area in Figure 7d−g. The target in Figure 7a has an overall diameter of 4.25 cm with an anisoplanatism factor of $\theta_s/\theta_t = 1.22$. The annular rings are 0.2 cm wide with a 0.15 cm spacing between adjacent rings. This corresponds to $\Delta l_t/\Delta l_s = 7.76$ equivalent to an imaging system with the same D/r_0. The reconstructed result without ACI is shown in Figure 7b. Tip-tilt and higher order aberrations have heavily disrupted the overall geometric shape of the target, and the target is barely recognizable. In general, partial retention of the structure permits restoration of near diffraction-limited imaging with approaches such as wavefront sensing-based adaptive optics[39,40] or deep learning methods.[89] However, the performance is considerably worse under deteriorating turbulence conditions. For example, increased

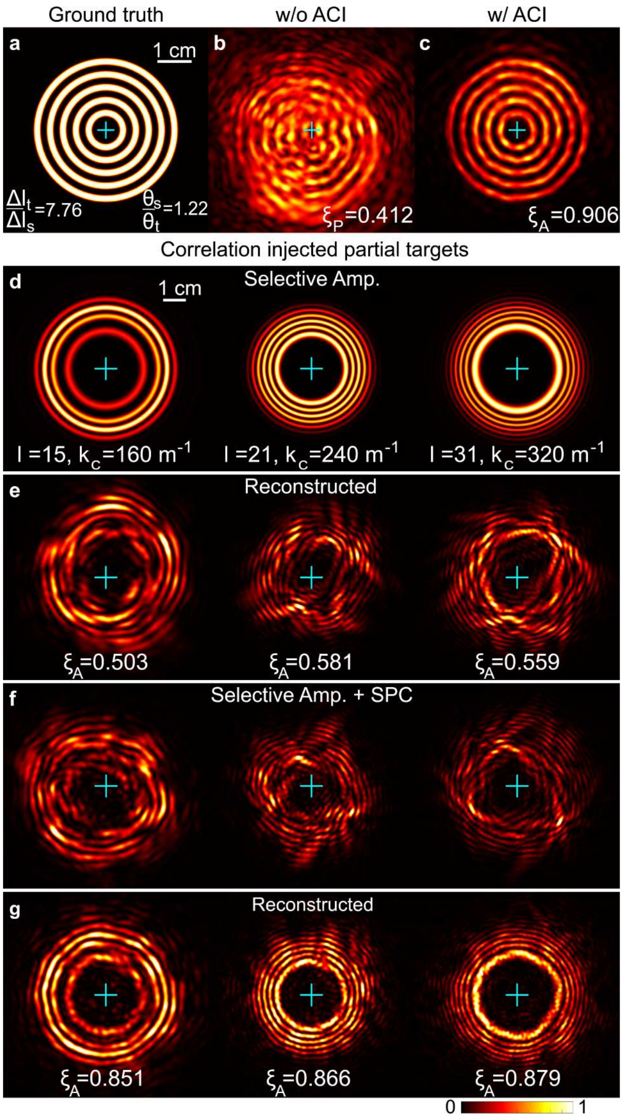

Figure 7. Wave propagation of a concentric ring target with and without the ACI framework for $C_n^2 = 1.5 \times 10^{-14}$ m$^{-2/3}$. (a) The target has feature sizes 7.76 times smaller than the resolution limit of the turbulent atmosphere under anisoplanatic conditions. The corresponding reconstructed intensity (b) without ACI has suffered severe geometric deformation and results in a poor ξ_P. (c) In contrast, with ACI, the reconstructed result retains the original geometric shape and yields a considerably higher ξ_A. This overall behavior of the SA and SPC methods under anisoplanatic conditions is studied with panels d−g using the OAM modes j = 2, 3, and 4 in Table 1.

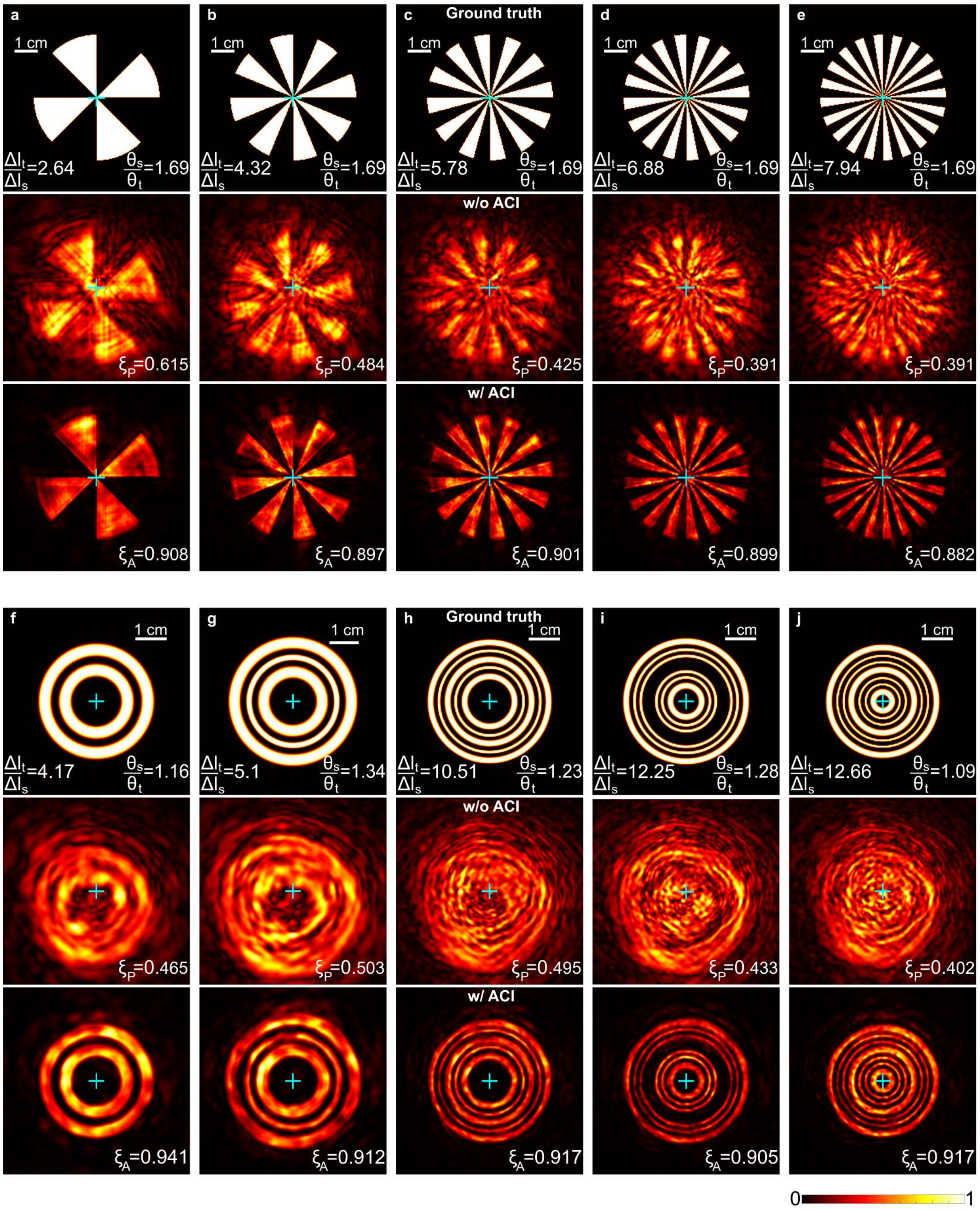

Figure 8. Comparison of wave propagation with and without ACI for arbitrary targets of varying complexities at $C_n^2 = 1.5 \times 10^{-14} \mathrm{m}^{-2/3}$. Reconstructed results for five Siemens star targets having four to 20 spokes are shown in (a)-(e), and five concentric ring targets with arbitrarily selected configurations are shown in (f) to (j). Tip-tilt and higher order aberrations progressively degrade reconstruction with increasing $\Delta l_t/\Delta l_s$. The overall geometric shape is recognizable for $\Delta l_t/\Delta l_s < 8$, since the higher order effects are not too dominant. In contrast, robust distortion suppression with ACI leads to high reconstruction fidelity with $\xi_A > 0.88$. Original geometric shape of each target is clearly distinguishable with a remarkably high contrast.

higher order aberration effects, severe scintillation, and higher branch point density[36] reduce the reliability of spatial domain wavefront sensing approaches[40] and are common when $\sigma_\chi^2 \geq 0.1$.[36,37] Since these effects increase in severity with worsening turbulence conditions, adaptable wavefront sensing approaches are often necessary to avoid focal spot higher order effects.[40] The reconstructed result with ACI is shown in Figure 7c. Strong suppression of both tilt and higher order aberration effects is clear. The concentric rings are visible with good contrast, and the overall pattern is centered around the optical axis (see the blue cross). This yields a higher ξ_A compared to ξ_P. This result suggests an overall resilience to turbulence-induced aberrations with the integration of the SA and SPC methods. We probe this further by systematically studying the wave propagation behavior of the correlation-injected partial targets in eq 9. The results are presented in Figure 7d−g for the OAM modes corresponding to j = 2, 3, and 4 in Table 1.

A critical part of ACI here is segmenting a broadband spatial frequency range into a set of narrow spectral bands, and this is achieved by sampling the broadband spectrum with the individually optimized OAM beams. Therefore, Gaussian

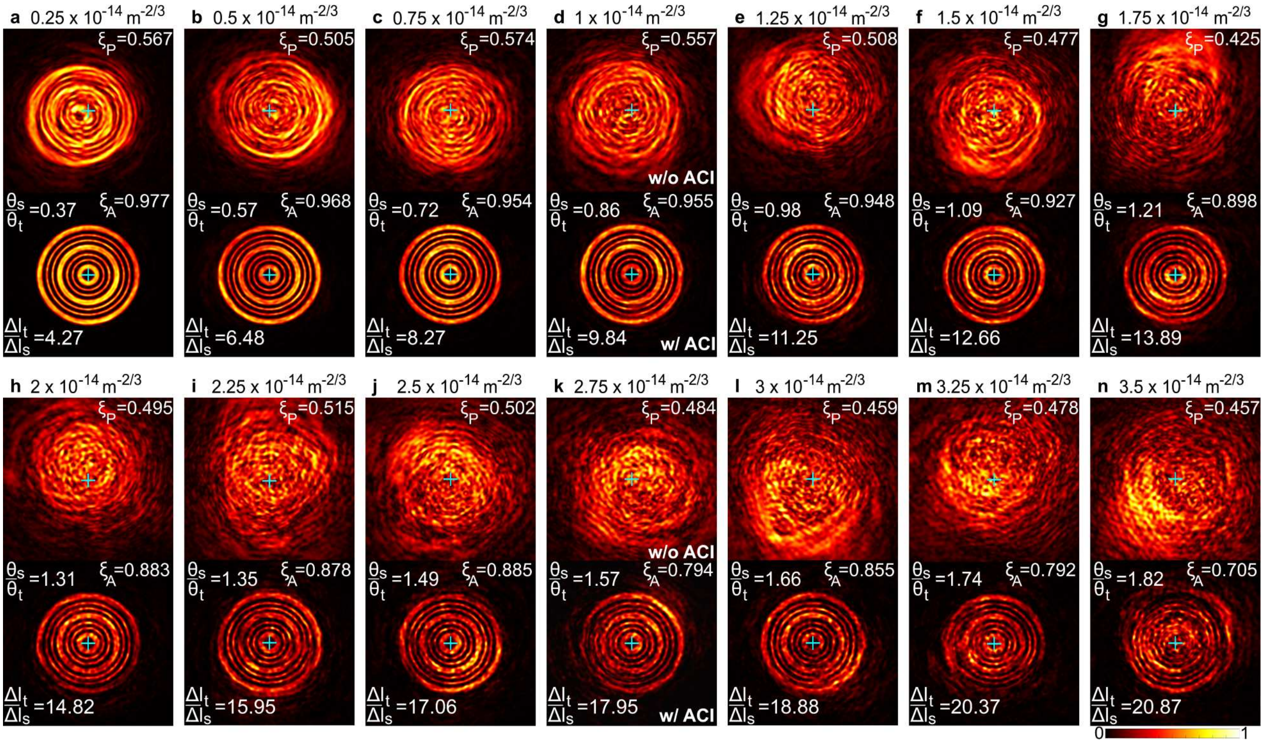

Figure 9. Comparison of wave propagation with and without ACI for increasing C_n^2 from 0.25 × 10^{-14} $m^{-2/3}$ in panel a to 3.5 × 10^{-14} $m^{-2/3}$ in panel n. The high complexity of the selected target renders it very vulnerable to distortions. Passive wave propagation rapidly deteriorates and the target is barely recognizable at $\Delta l_t/\Delta l_s = 8.27$ where $C_n^2 = 0.75 \times 10^{-14} m^{-2/3}$ as seen in panel c. In contrast, the active system exhibits remarkable tolerance to aberrations and relatively high ξ_A is maintained up to approximately $C_n^2 = 3.5 \times 10^{-14} m^{-2/3}$ where $\Delta l_t/\Delta l_s = 20.87$.

beams alone are not suitable for this purpose. We only use one super-Gaussian beam for the SPC at the lowest spatial frequencies (i.e., $V_0(\mathbf{k})$ in Table 1). The Gaussian beams could be used to correct beam wandering, which is important to prevent fading in FSO communications, but this can be addressed with adaptive optics more easily. The ACI is concerned with the high-fidelity transmission of complex beams with finer spatial features.

Consider now the effect of anisoplanatism on the efficacy of CIS from the previous discussion. In principle, $\rho_j(\mathbf{r})$ contains a conjugate of the characterized turbulence-induced aberration for the selected bandwidth. Through the convolution in eq 9, the jth CIS (i.e., $\nu_j(\mathbf{r}) * \rho_j(\mathbf{r})$) is injected into the target. However, the unknown power spectral density distribution of the target implies a different physical space mode profile of $|o(\mathbf{r}) * \nu_j(\mathbf{r})|^2$ compared with $|\nu_j(\mathbf{r})|^2$. This is shown in Figure 7d, which plots the normalized $|o(\mathbf{r}) * \nu_j(\mathbf{r})|^2$ for the selected OAM modes. Consequently, a small difference in the diffraction cones between $o(\mathbf{r}) * \nu_j(\mathbf{r})$ and $\nu_j(\mathbf{r})$ is expected as well as by extension an additional deviation from the characterized aberration due to anisoplanatism. This is expected to further compromise the conjugate of the distortion carried out by $\rho_j(\mathbf{r})$. The question that arises is the impact of anisoplanatism and how the angular size of the selected target affects the performance of the jth injected partial target. The reconstructed result after propagating $o(\mathbf{r}) * \nu_j(\mathbf{r})$ through turbulence is shown in Figure 7e. The correlation-injected targets with selective amplification and SPC are shown in Figure 7f. The corresponding reconstructed results after propagation through turbulence are shown in Figure 7g. Wave propagation fidelity is clearly improved (similar to the discussion associated with Figures 4 and 5) indicating that the estimated CIS $\rho_j(\mathbf{r})$ retains strong effectiveness. However, the slight loss in effectiveness of the generated CIS is also evident from the slightly lower values of ξ_A compared to the results in Figure 5b for the same C_n^2. Note that controlling the mode parameters in eq 4 offers some limited degree of freedom to reduce the impact of anisoplanatism. However, despite this limitation, the procedure still yields a sufficiently strong enhancement in ξ_A particularly for the high spatial frequency modes, which are more sensitive to distortion. In principle, spatial domain wavefront correction approaches[105,106] can be applied to the reconstructed targets in Figure 7g, leading to further enhancement in Figure 7c. If the angular size of the target is unknown or for a desired imaging FOV, a more robust formulation of eq 6 can be formulated by factoring in the effect of anisoplanatism. One possible way could entail transforming eq 9 into a superposition integral to generate $o_{j,\mathrm{A}}(\mathbf{r})$. The convolution term can be substituted with

$$o_{j,\mathrm{A}}(\mathbf{r}) = \sum_m o(\mathbf{r}) * \nu_j(\mathbf{r}) * \rho_{j,m}(\mathbf{r}) \tag{15}$$

where $\rho_{j,m}(\mathbf{r})$ is the CIS for the mth spatial segment of the desired imaging FOV.

We now generalize the analysis described above with more complex arbitrary targets under varying turbulence strengths. The optimized OAM beam parameters and the underlying postprocessing algorithm are unchanged. Initially, we continue with $C_n^2 = 1.5 \times 10^{-14}$ $m^{-2/3}$ and a single realization of the stochastic spatially varying refractive index distribution is assumed. This enables the continuation of the previous analysis with diverse field distributions. Then, the propagation of one target with a relatively high complexity will be studied for increasing C_n^2.

The collage in Figure 8 compares the wave propagation behavior of five Siemens star and concentric ring type spatial field distributions with and without ACI at $C_n^2 = 1.5 \times 10^{-14}\text{m}^{-2/3}$. Each subfigure shows the normalized spatial intensity distribution over a 6×6 cm^2 area. The reconstructed results without and with ACI are shown in the second and third rows, respectively, in each subfigure. The complexity of wave propagation for each target is quantified with $\Delta l_t/\Delta l_s$ and θ_s/θ_t. Therefore, the Siemens star targets in Figure 8a−e will experience stronger anisoplanatism relative to the concentric ring targets in Figure 8f−j. The diameter of each Siemens star is 6.02 cm, and the target complexity is increased by incrementing the number of spokes from 4 to 20 as shown in Figure 8a−e. For the concentric ring targets, the width and separations between each annular ring are arbitrarily adjusted to control target complexity. Note that the selected target parameters diversifies the observed severity of tip-tilt and higher order aberrations for the same turbulence strength and tests the effectiveness of the ACI framework.

The passively reconstructed results exhibit progressively severe tip-tilt and higher order aberrations with increasing target complexity. In certain cases, the distortion is not severe enough, and the reconstructions retain some of the original geometric features, such as the number of spokes. In general, this observation is more or less maintained when $\Delta l_t/\Delta l_s < 8$. The original shape, though heavily disrupted, is still partially recognizable and could be restored with established correction techniques involving adaptive optics or machine learning. However, when $\Delta l_t/\Delta l_s > 8$, the turbulence aberrations are significantly more dominant as is evident from Figure 8h−j. The original geometric pattern is unrecognizable. Overall, poor wave propagation fidelity is noted with the highest $\xi_P = 0.615$ in Figure 8a.

In contrast, the reconstructed results with ACI show a remarkable enhancement for all selected targets in Figure 8. The original spatial mode structure of each target is well preserved after propagation and it is possible to resolve the smallest features with good contrast. Strong suppression of both tip-tilt and higher order aberrations is clearly evident. Each reconstructed result with ACI shows consistently high values of ξ_A over ξ_P. It is worth highlighting that the OAM mode parametrization, previously optimized with a different target retains very strong enhancement in ξ_A. Therefore, the parametrization for a given reciprocal space bandwidth can be considered as a one time calibration process. Robust distortion mitigation is possible with a diverse range of targets provided that their power spectral density is reasonably well covered by the parametrized OAM modes.

We now expand on the previous analysis and investigate the performance of the ACI under increasingly strong turbulent conditions. This is achieved by studying the wave propagation behavior with and without ACI within $2.5 \times 10^{-15} \leq C_n^2 \leq 3.5 \times 10^{-14}$ m$^{-2/3}$ and comparing the enhancement of ξ_A over ξ_P. We consider the concentric ring target in Figure 8j due to its high complexity and vulnerability to turbulence distortions. For each C_n^2, a set of ten phase screens from a random draw are generated for numerical wave propagation. The results are presented in the collage in Figure 9 where normalized spatial intensity distributions are plotted over a 6×6 cm^2 area in each subfigure. The passive and active reconstructed results are shown in the first and second rows for each subfigure. Note that in Figures 9a−e, since θ_s/θ_t is less than unity, wave propagation is approximately isoplanatic. However, due to the high complexity of the target, the passive reconstructed result is more or less unrecognizable at $\Delta l_t/\Delta l_s = 8.27$ where $C_n^2 = 0.75 \times 10^{-14}$ m$^{-2/3}$ as is evident in Figure 9c. In contrast, the active reconstructed results continue to show a strong enhancement, and a remarkably high contrast between the concentric rings is observable. Under approximately isoplanatic conditions, the underlying system approaches a linear shift invariant wave propagation behavior. Therefore, the estimated CISs retain maximum effectiveness when the distortion corrections are injected into each partial target with eq 9. Consequently, the reconstructed results show very high NCC with $\xi_A > 0.94$. With further increments to C_n^2, the passive reconstruction is entirely unrecognizable due to strong tilt and higher order aberrations. With the onset of anisoplanatism, the performance of ACI is reduced for increasing target complexity, but robust wave propagation is still maintained. The reconstructed results continue to exhibit high NCC as is evident from the second rows in Figure 9f−n. The reconstructed results exhibit reasonably good contrast, and it is possible to clearly resolve the thinnest concentric rings. However, at $C_n^2 = 3.5 \times 10^{-14}$ m$^{-2/3}$, $r_0 = 6.67$ cm, $\sigma_\chi^2 = 0.07$, and the corresponding $\Delta l_t = 2.84$ cm, which is more than 20 times larger than the resolution of the simulated target. This is equivalent to imaging with $D/r_0 > 20$. The additional effect of anisoplanatism under strong aberration severely undermines the effectiveness of the CISs and the estimated distortion corrections.

The analysis presented with Figures 8 and 9 offers detailed insights regarding the ACI framework, and several key conclusions can be drawn. First, with a robust initial reciprocal space calibration of the OAM mode similar to Table 1, the framework can potentially maintain robust distortion mitigation even when both the target and environmental propagation conditions change while continuous acquisitions are performed. However, the CISs need to be continually generated for each data acquisition step. Second, stable performance over a relatively wide range of C_n^2 also implies that the system could require fewer recalibrations to adapt to prevailing turbulence conditions. Third, distortion estimation with guide stars or pilot beams was commonly used in diverse fields when long propagation paths through turbulence or deep-tissue imaging through a scattering and a turbulent biological sample are desired.[18−21] The formulation of a hybrid technique, for example, with a combination of traditional physical space and ACI's reciprocal space distortion estimation technique followed by correlation injection could propel the hybrid method into more challenging domains independently inconceivable with either technique.

■ DISCUSSION AND CONCLUSION

To implement the ACI, we need to gain information about how the atmosphere distorts the spectral phase distribution over a set of narrow spatial frequency bands before the atmosphere decorrelates. Therefore, in the characterization stage (Figure 3a), we use a set of optimized OAM beams to probe the atmosphere. The optimization of the OAM beams (see Table 1) along with that of the corresponding window functions (see eqs 11 and 12) using a calibration target is a one-time process. In this work, the optimization is performed for $C_n^2 = 1.5 \times 10^{-14}$ m$^{-2/3}$ and a radially symmetric calibration target. However, testing the same set of OAM beams and window functions with different targets and C_n^2 values gives surprisingly high-quality reconstructions as seen in Figures 8, 9,Section S2, and Figures S8 and S9 despite arbitrary input shapes, amplitude, and phase. This suggests that the ACI is highly object-independent within the system-specific anisoplanatism and resolution limits.

The results emphasize the enhancement achievable with ACI's active optical compensation technique with correlation-injected auxiliary sources whenever high wave propagation fidelity through a turbulent medium is desirable. The present theoretical framework suggests that robust distortion mitigation up to $C_n^2 = 3.5 \times 10^{-14}$ m$^{-2/3}$ or equivalently for $D/r_0 \approx 20$ under moderately anisoplanatic conditions is a possibility. The enhancement can be furthered first with a more robust alternative to the OAM beam $v(\mathbf{r})$ and second by accounting for anisoplanatism in the spectral distortion characterization detailed in eq 6. The present work uses only the spatial amplitude and phase profile of the OAM beam for the characterization. In principle, tilt, beam diameter, coherence, or polarization could also be included as additional degrees of freedom since they are known to be sensitive to wave propagation through turbulence.[61,107] The orthogonal mode sets of the Laguerre−Gaussian, Bessel, Hermite−Gaussian, Ince−Gaussian,[108] or their vectorial combinations[109−112] could be used as potential alternatives to the OAM beam used in this work. The turbulence resilience[112,113] of the above modes is questionable.[97,114] However, employing them for spectral distortion characterization to generate a CIS does not necessarily require good turbulence resilience. Interestingly, the inhomogeneous polarization of vectorial fields exhibits more tolerance to turbulence[59] relative to the spatial mode structure of the beam. Therefore, further enhancement could be possible by injecting an encoded CIS into the polarization profile[115] rather than the complex field with the corresponding modification to the observation plane detection process.[112,116]

The use of self-healing fields such as Airy or Bessel beams[100,117] could be beneficial to counter the impact of optical beam divergence. Using such beams as a probe for characterization or during the correlation injection stage could be possible. However, employing such beams particularly in long-range telecommunications is challenging, since the width of the beam is directly proportional to the desired propagation length.[61] This would require larger beam sizes in the source plane. A possible alternative could be the deployment of partially coherent self-focusing fields carrying OAM.[100] The self-focusing property in both free space and oceanic turbulence makes them viable candidates for FSO communication links[61] and could be used instead of the OAM modes in the present work. The effect of beam divergence on the CIS generation and the performance of ACI, based on the OAM modes considered in this work, has been analyzed in Section S6 and the provided Supporting Information animation movie.

While all structured light beams are adversely affected by turbulence, with optimal and precise manipulation, the turbulence-induced effects on structured beams can be utilized as signatures[118] to enhance ACI's spectral distortion characterization. Consequently, extension of ACI into stronger turbulence regimes with anisotropic, inhomogeneous index fluctuations and deep turbulence effects[119] and biomedical imaging could be possible. Biological tissues exhibit refractive index inhomogeneities similar to atmospheric turbulence with unique power spectra models.[38,120] Beam spreading, wandering, and higher order effects influence the spot size, energy radiation, and beam directionality.[121,122] This often disrupts deep tissue imaging, since the Rytov variance rapidly enters a strong turbulence regime within a 30 μm penetration depth.[38] This limits the scope and impact of super-resolution imaging techniques such as SIM, STED, PALM, and so on.[17] The ongoing research on adaptive optics integration[123,124] could be complemented with the ACI framework to enable more comprehensive views of increasingly complex neurobiological samples maintained in a physiological state. In principle, the diverse experimental configurations of guide stars used for adaptive optics or wavefront shaping implementations for various applications[34,35,43,49−51] could also be employed to formulate ACI's reciprocal space distortion characterization.

In order to implement the ACI method into an experimental system, it is necessary to implement the convolution detailed in eqs 7 and 9. The selected OAM mode profile can be generated using spatial light modulators,[125] spiral phase plates,[126,127] forked[128] or phase diffractive vortex gratings,[129,130] and metasurfaces[131,132] when system miniaturization or nanometer-scale optical manipulation is important. OAM modes have become a popular and rapidly evolving field and advances in available generation technologies for various wavelengths are discussed in recent reviews.[133−136] The convolution between an arbitrary field and the OAM mode could be implemented as a reciprocal space product.[78] The CIS can be generated by first extracting the phase information using existing holographic or interferometric techniques. Recent advances on metasurface phase change materials offering electrical tunability,[137] high spatial scalability (up to nanometer scales), and fast switching speed[138−140] could be potential candidates to implement the CIS beam. It is not necessary to have direct access to the distal side of the medium. In that case, the present implementation requires optical convolution at a distance from the target. This may involve round-trip propagations of the OAM beam and scanning the target with the corrected OAM beams, the details of which depend on the given system. Such tasks can be relatively easier in FSO communication applications since we can have access to both sides of the channel for feedback. Therefore, our technique has the potential to provide an advantage regardless of access to the distal side.

The frozen turbulence assumption used in the theoretical framework requires some consideration. The effectiveness of the CIS and consequently the achievable distortion mitigation decay over time as the medium evolves from the moment of characterization. Therefore, the CIS would require periodic reconfiguration to maintain a desirable enhancement. The reconfiguration latency would depend on the nature of the dynamic turbulent medium and the propagation distance. For example phase fluctuations caused by atmospheric turbulence rarely evolve faster than 10 ms.[141] Therefore, a 1 ms latency[33] could be sufficient. In contrast, active turbulence from physiological motion in live biological tissues causes phase fluctuations to evolve at 1 ms or less and would require considerably smaller latency[142] between CIS updates.

Although rapid developments in novel wavefront shaping technologies show promising potential, low latency CIS reconfiguration is a challenge that should not be downplayed, as the correlation time is sensitive to the dynamic turbulent medium. Periodic reconfiguration of the CIS in ACI with a low latency requires rapid sequential completion of the three stages illustrated in Figure 3a. These stages share similarities in terms of reconfigurability with the typical wavefront measurement and compensation stages used with adaptive optics and wavefront shaping techniques. The wavefront measurements can require many iterations to find a satisfactory modulation wavefront within a reasonable latency in highly dynamic turbulent media.[19] This can sometimes dominate the subsequent compensation process.[143] In contrast, ACI's measurement stage could be performed faster since it does not require real-time optimization. Having said that, wavefront shaping in complex media with a system latency as fast as about 10 μs has recently been demonstrated with a photorefractive crystal-based analogue of optical phase conjugation.[142] Single-shot wavefront measurements with a latency of 1 ms have been demonstrated.[143] Because these parameters are dependent on the specific implementation or probe beam configuration, the true system latency should be determined based on a specific ACI application. Nonetheless, the targets propagated with ACI can maintain a considerably high fidelity in the original geometric structure as the atmosphere decorrelates (Section S4). Interestingly, a potential solution may be found in a recent experimental work involving superresolution imaging in dynamic scattering media with strong decorrelation times.[144] Machine learning could also be used to anticipate future reconfigurations to the CIS beam.[93,145] One immediate research that can benefit from ACI is in remote sensing through a turbulent atmosphere. For example, ACI can allow for the formation of high-fidelity Moiré fringes to enable enhanced remote sensing of seismological signals.[146]

Finally, FSO communication is an active research area to enable high speed communication systems where laying fiber is not an appropriate option.[147,148] One of the active research areas within FSO is exploring how to utilize the space within the communication link as effectively as possible[62,103,148−150] with Laguerre−Gaussian modes, Hermite−Gaussian modes, and linearly polarized modes, currently providing the leading mode capacity.[150] Spatial mode multiplexing with ACI does not necessarily require orthogonal mode sets, which are prone to crosstalk in turbulence, but rather offers a novel way of efficient multiplexing based on spatial encoding.[62] ACI can allow for distinct high-density channels within a communication link, even in the presence of turbulence comparable to the turbulence-free theoretical limit of the state-of-the-art FSO communication systems, as illustrated in Section S5. Achieving the same result with the orthogonal states poses stringent requirements of form invariance.[62,63]

In conclusion, we have presented the first framework for enhancing complex wave propagation through turbulent media with the ACI technique. A theoretical description of the proposed framework is developed for coherent light and extensively tested with numerical simulations. The proposed method can provide high-fidelity propagation through a turbulent medium up to $D/r_0 \approx 20$ under anisoplanatic conditions. We have outlined several potential strategies to further extend the framework into stronger and dynamic turbulence regimes. The results underscore the high versatility and ubiquity of the concepts behind ACI (e.g., selective amplification, virtual gain, and correlation injection), applicable to a wide range of distinct distortion or noise mitigation problems spanning from shot noise to turbulent medium and from nanoimaging to atmospheric propagation. Our work may stimulate new research in the broad applications of statistical sciences.

■ ASSOCIATED CONTENT

Supporting Information

The Supporting Information is available free of charge at https://pubs.acs.org/doi/10.1021/acsphotonics.4c00687.

Numerical model that emulates wave propagation through a turbulent atmosphere; ACI performance with target asymmetry and phase; spatial and temporal coherence; ACI performance under finite reconfiguration latency; spatial mode multiplexing with ACI; the effect of beam divergence on the ACI performance (PDF)

Effect of beam divergence on the CIS generation and the performance of ACI based on the OAM modes (MPG)

■ AUTHOR INFORMATION

Corresponding Author

Durdu Ö. Güney − *Department of Electrical and Computer Engineering, Michigan Technological University, Houghton, Michigan 49931-1295, United States; John A. Paulson School of Engineering and Applied Sciences, Harvard University, Cambridge, Massachusetts 02138, United States;* orcid.org/0000-0002-6734-7469; Email: dguney@mtu.edu

Authors

Anindya Ghoshroy − *Department of Electrical and Computer Engineering, Michigan Technological University, Houghton, Michigan 49931-1295, United States*

James Davis − *Department of Electrical and Computer Engineering, Michigan Technological University, Houghton, Michigan 49931-1295, United States*

Adrian A. Moazzam − *Department of Electrical and Computer Engineering, Michigan Technological University, Houghton, Michigan 49931-1295, United States*

Roohollah Askari − *Geological and Mining Engineering and Sciences, Michigan Technological University, Houghton, Michigan 49931-1295, United States*

Complete contact information is available at: https://pubs.acs.org/10.1021/acsphotonics.4c00687

Funding

This work was supported by the National Science Foundation (EAR-2221730).

Notes

The authors declare no competing financial interest.

■ ACKNOWLEDGMENTS

The authors thank Jeremy Bos at Michigan Technological University for fruitful discussions.

■ REFERENCES

(1) Inavalli, V. K.; Lenz, M. O.; Butler, C.; Angibaud, J.; Compans, B.; Levet, F.; Tønnesen, J.; Rossier, O.; Giannone, G.; Thoumine, O. A super-resolution platform for correlative live single-molecule imaging and STED microscopy. *Nat. Methods* **2019**, *16*, 1263−1268.

(2) Zhang, H.; Shao, S.; Sun, Y. Characterization of liquid−liquid phase separation using super-resolution and single-molecule imaging. *Biophys. Rep.* **2022**, *8*, 2−13.

(3) Li, X.; Wu, Y.; Su, Y.; Rey-Suarez, I.; Matthaeus, C.; Updegrove, T. B.; Wei, Z.; Zhang, L.; Sasaki, H.; Li, Y.; et al. Three-dimensional structured illumination microscopy with enhanced axial resolution. *Nat. Biotechnol.* **2023**, *41*, 1307−1319.

(4) Johansson, B.; Oasa, S.; Muntsant Soria, A.; Tiiman, A.; Söderberg, L.; Amandius, E.; Möller, C.; Lannfelt, L.; Terenius, L.; Giménez-Llort, L.; et al. The interwoven fibril-like structure of amyloid-beta plaques in mouse brain tissue visualized using super-resolution STED microscopy. *Cell Biosci.* **2023**, *13*, 142.

(5) Calovi, S.; Soria, F. N.; Tønnesen, J. Super-resolution STED microscopy in live brain tissue. *Neurobiol. Dis.* **2021**, *156*, 105420.

(6) Hugelier, S.; Colosi, P.; Lakadamyali, M. Quantitative Single-Molecule Localization Microscopy. *Annu. Rev. Biophys.* **2023**, *52*, 139−160.

(7) Park, S.; Jo, Y.; Kang, M.; Hong, J. H.; Ko, S.; Kim, S.; Park, S.; Park, H. C.; Shim, S.-H.; Choi, W. Label-free adaptive optics single-molecule localization microscopy for whole zebrafish. *Nat. Commun.* **2023**, *14*, 4185.

(8) Hou, Y.; Laasmaa, M.; Li, J.; Shen, X.; Manfra, O.; Nordén, E. S.; Le, C.; Zhang, L.; Sjaastad, I.; Jones, P. P. Live-cell photoactivated localization microscopy correlates nanoscale ryanodine receptor configuration to calcium sparks in cardiomyocytes. *Nat. Cardiovasc. Res.* **2023**, *2*, 251−267.

(9) Basumatary, J.; Baro, N.; Joshi, P.; Mondal, P. P. Scanning single molecule localization microscopy (scanSMLM) for super-resolution volume imaging. *Commun. Biol.* **2023**, *6*, 1050.

(10) Hess, S. T.; Girirajan, T. P.; Mason, M. D. Ultra-high resolution imaging by fluorescence photoactivation localization microscopy. *Biophys. J.* **2006**, *91*, 4258−4272.

(11) Rust, M. J.; Bates, M.; Zhuang, X. Sub-diffraction-limit imaging by stochastic optical reconstruction microscopy (STORM). *Nat. Methods* **2006**, *3*, 793−796.

(12) Jelken, J.; Lambin, C.; Avilés, M. O.; Lagugné-Labarthet, F. Real-time observation of photo-oxidation of single MoS_2 flakes using stochastic optical reconstruction microscopy. *J. Phys. Chem. C* **2023**, *127*, 14270−14282.

(13) Ando, T.; Bhamidimarri, S. P.; Brending, N.; Colin-York, H.; Collinson, L.; De Jonge, N.; De Pablo, P.; Debroye, E.; Eggeling, C.; Franck, C. The 2018 correlative microscopy techniques roadmap. *J. Phys. D: Appl. Phys.* **2018**, *51*, 443001.

(14) Pope, I.; Tanner, H.; Masia, F.; Payne, L.; Arkill, K. P.; Mantell, J.; Langbein, W.; Borri, P.; Verkade, P. Correlative light-electron microscopy using small gold nanoparticles as single probes. *Light: Sci. Appl.* **2023**, *12*, 80.

(15) Tanner, H.; Sherwin, O.; Verkade, P. Labelling strategies for correlative light electron microscopy. *Microsc. Res. Technol.* **2023**, *86*, 901−910.

(16) Richardson, D. J.; Fini, J. M.; Nelson, L. E. Space-division multiplexing in optical fibres. *Nat. Photonics* **2013**, *7*, 354−362.

(17) Arizono, M.; Idziak, A.; Quici, F.; Nägerl, U. V. Getting sharper: The brain under the spotlight of super-resolution microscopy. *Trends Cell Biol.* **2023**, *33*, 148−161.

(18) Mosk, A. P.; Lagendijk, A.; Lerosey, G.; Fink, M. Controlling waves in space and time for imaging and focusing in complex media. *Nat. Photonics* **2012**, *6*, 283−292.

(19) Bertolotti, J.; Katz, O. Imaging in complex media. *Nat. Phys.* **2022**, *18*, 1008.

(20) Ntziachristos, V. Going deeper than microscopy: The optical imaging frontier in biology. *Nat. Methods* **2010**, *7*, 603−614.

(21) Yoon, S.; Cheon, S. Y.; Park, S.; Lee, D.; Lee, Y.; Han, S.; Kim, M.; Koo, H. Recent advances in optical imaging through deep tissue: Imaging probes and techniques. *Biomater. Res.* **2022**, *26*, 57.

(22) Li, H.; Hao, Z.; Huang, J.; Lu, T.; Liu, Q.; Fu, L. 500 μm field-of-view probe-based confocal microendoscope for large-area visualization in the gastrointestinal tract. *Photonics Res.* **2021**, *9*, 1829−1841.

(23) Theer, P.; Hasan, M. T.; Denk, W. Two-photon imaging to a depth of 1000 μm in living brains by use of a Ti: Al_2O_3 regenerative amplifier. *Opt. Lett.* **2003**, *28*, 1022−1024.

(24) Wang, T.; Xu, C. Three-photon neuronal imaging in deep mouse brain. *Optica* **2020**, *7*, 947−960.

(25) Horton, N. G.; Wang, K.; Kobat, D.; Clark, C. G.; Wise, F. W.; Schaffer, C. B.; Xu, C. In vivo three-photon microscopy of subcortical structures within an intact mouse brain. *Nat. Photonics* **2013**, *7*, 205−209.

(26) Badon, A.; Li, D.; Lerosey, G.; Boccara, A. C.; Fink, M.; Aubry, A. Smart optical coherence tomography for ultra-deep imaging through highly scattering media. *Sci. Adv.* **2016**, *2*, No. e1600370.

(27) Cao, J.; Yang, Q.; Miao, Y.; Li, Y.; Qiu, S.; Zhu, Z.; Wang, P.; Chen, Z. Enhance the delivery of light energy ultra-deep into turbid medium by controlling multiple scattering photons to travel in open channels. *Light: Sci. Appl.* **2022**, *11*, 108.

(28) Yang, Q.; Cao, J.; Miao, Y.; Zhu, J.; Chen, Z. Extended imaging depth of en-face optical coherence tomography based on fast measurement of a reflection matrix by wide-field heterodyne detection. *Opt. Lett.* **2020**, *45*, 828−831.

(29) Yang, Q.; Miao, Y.; Huo, T.; Li, Y.; Heidari, E.; Zhu, J.; Chen, Z. Erratum: "Deep imaging in highly scattering media by combining reflection matrix measurement with Bessel-like beam based optical coherence tomography" [Appl. Phys. Lett. 113 , 011106 (2018)]. *Appl. Phys. Lett.* **2018**, *113*, 109901.

(30) Rotter, S.; Gigan, S. Light fields in complex media: Mesoscopic scattering meets wave control. *Rev. Mod. Phys.* **2017**, *89*, 015005.

(31) Zhou, S.; Zhang, Q.; Gao, R.; Chang, H.; Xin, X.; Li, S.; Pan, X.; Tian, Q.; Tian, F.; Wang, Y. High-accuracy atmospheric turbulence compensation based on a Wirtinger flow algorithm in an orbital angular momentum-free space optical communication system. *Opt. Commun.* **2020**, *477*, 126322.

(32) Hao, Y.; Xiao, Y.; Chen, W. High-fidelity ghost diffraction through complex scattering media using a modified Gerchberg-Saxton algorithm. *Opt. Express* **2023**, *31*, 14389−14402.

(33) Rukosuev, A.; Nikitin, A.; Toporovsky, V.; Sheldakova, J.; Kudryashov, A. Real-time correction of a laser beam wavefront distorted by an artificial turbulent heated airflow. *Photonics* **2022**, *9*, 351.

(34) Ji, N. Adaptive optical fluorescence microscopy. *Nat. Methods* **2017**, *14*, 374−380.

(35) Davies, R.; Kasper, M. Adaptive optics for astronomy. *Annu. Rev. Astron. Astrophys.* **2012**, *50*, 305−351.

(36) Beck, J. R.; Bos, J. P.; Brennan, T. J.; Spencer, M. F. Wave-optics investigation of branch-point density. *Opt. Eng.* **2022**, *61*, 044104−044104.

(37) Kalensky, M. Branch-point identification using second-moment Shack−Hartmann wavefront sensor statistics. *Appl. Opt.* **2023**, *62*, G101−G111.

(38) Gökçe, M. C.; Ata, Y.; Baykal, Y. Tissue turbulence and its effects on optical waves: A review. *Opt. Commun.* **2023**, *546*, 129816.

(39) Barchers, J. D.; Fried, D. L.; Link, D. J. Evaluation of the performance of Hartmann sensors in strong scintillation. *Appl. Opt.* **2002**, *41*, 1012−1021.

(40) Lechner, D.; Zepp, A.; Eichhorn, M.; Gładysz, S. Adaptable Shack-Hartmann wavefront sensor with diffractive lenslet arrays to mitigate the effects of scintillation. *Opt. Express* **2020**, *28*, 36188−36205.

(41) Osnabrugge, G.; Horstmeyer, R.; Papadopoulos, I. N.; Judkewitz, B.; Vellekoop, I. M. Generalized optical memory effect. *Optica* **2017**, *4*, 886−892.

(42) Lai, P.; Wang, L.; Tay, J. W.; Wang, L. V. Photoacoustically guided wavefront shaping for enhanced optical focusing in scattering media. *Nat. Photonics* **2015**, *9*, 126−132.

(43) Vellekoop, I. M. Feedback-based wavefront shaping. *Opt. Express* **2015**, *23*, 12189−12206.

(44) Liu, L.; Liang, W.; Qu, Y.; He, Q.; Shao, R.; Ding, C.; Yang, J. Anti-scattering light focusing with full-polarization digital optical phase conjugation based on digital micromirror devices. *Opt. Express* **2022**, *30*, 31614−31622.

(45) Popoff, S. M.; Lerosey, G.; Carminati, R.; Fink, M.; Boccara, A. C.; Gigan, S. Measuring the transmission matrix in optics: An

approach to the study and control of light propagation in disordered media. *Phys. Rev. Lett.* **2010**, *104*, 100601.

(46) Luo, Y.; Yan, S.; Li, H.; Lai, P.; Zheng, Y. Focusing light through scattering media by reinforced hybrid algorithms. *APL Photonics* **2020**, *5*, 016109.

(47) Chaigne, T.; Katz, O.; Boccara, A. C.; Fink, M.; Bossy, E.; Gigan, S. Controlling light in scattering media non-invasively using the photoacoustic transmission matrix. *Nat. Photonics* **2014**, *8*, 58−64.

(48) Katz, O.; Ramaz, F.; Gigan, S.; Fink, M. Controlling light in complex media beyond the acoustic diffraction-limit using the acousto-optic transmission matrix. *Nat. Commun.* **2019**, *10*, 717.

(49) Boniface, A.; Dong, J.; Gigan, S. Non-invasive focusing and imaging in scattering media with a fluorescence-based transmission matrix. *Nat. Commun.* **2020**, *11*, 6154.

(50) Yang, J.; Li, L.; Shemetov, A. A.; Lee, S.; Zhao, Y.; Liu, Y.; Shen, Y.; Li, J.; Oka, Y.; Verkhusha, V. V.; et al. Focusing light inside live tissue using reversibly switchable bacterial phytochrome as a genetically encoded photochromic guide star. *Sci. Adv.* **2019**, *5*, No. eaay1211.

(51) Horstmeyer, R.; Ruan, H.; Yang, C. Guidestar-assisted wavefront-shaping methods for focusing light into biological tissue. *Nat. Photonics* **2015**, *9*, 563−571.

(52) Boniface, A.; Blochet, B.; Dong, J.; Gigan, S. Noninvasive light focusing in scattering media using speckle variance optimization. *Optica* **2019**, *6*, 1381−1385.

(53) Suzuki, Y.; Tay, J. W.; Yang, Q.; Wang, L. V. Continuous scanning of a time-reversed ultrasonically encoded optical focus by reflection-mode digital phase conjugation. *Opt. Lett.* **2014**, *39*, 3441−3444.

(54) Wang, Y. M.; Judkewitz, B.; DiMarzio, C. A.; Yang, C. Deep-tissue focal fluorescence imaging with digitally time-reversed ultrasound-encoded light. *Nat. Commun.* **2012**, *3*, 928.

(55) Cao, J.; Yang, Q.; Miao, Y.; Li, Y.; Wang, P.; Chen, Z. High-speed wavefront determination method based on single in-and-out electric field analysis to focus light through highly scattering medium. *APL Photonics* **2021**, *6*, 036107.

(56) Cox, M. A.; Mphuthi, N.; Nape, I.; Mashaba, N.; Cheng, L.; Forbes, A. Structured light in turbulence. *IEEE J. Sel. Top. Quantum Electron.* **2021**, *27*, 1−21.

(57) Forbes, A.; de Oliveira, M.; Dennis, M. R. Structured light. *Nat. Photonics* **2021**, *15*, 253−262.

(58) Forbes, A. Structured light: Tailored for purpose. *Opt. Photon. News* **2020**, *31*, 24−31.

(59) Nape, I.; Singh, K.; Klug, A.; Buono, W.; Rosales-Guzman, C.; McWilliam, A.; Franke-Arnold, S.; Kritzinger, A.; Forbes, P.; Dudley, A. Revealing the invariance of vectorial structured light in complex media. *Nat. Photonics* **2022**, *16*, 538−546.

(60) Lavery, M. P. Vortex instability in turbulent free-space propagation. *New J. Phys.* **2018**, *20*, 043023.

(61) Luo, M.; Koivurova, M.; Ornigotti, M.; Ding, C. Turbulence-resistant self-focusing vortex beams. *New J. Phys.* **2022**, *24*, 093036.

(62) Klug, A.; Peters, C.; Forbes, A. Robust structured light in atmospheric turbulence. *Adv. Photonics* **2023**, *5*, 016006−016006.

(63) Bachmann, D.; Isoard, M.; Shatokhin, V.; Sorelli, G.; Treps, N.; Buchleitner, A. Highly transmitting modes of light in dynamic atmospheric turbulence. *Phys. Rev. Lett.* **2023**, *130*, 073801.

(64) Zhang, R.; Hu, N.; Zhou, H.; Zou, K.; Su, X.; Zhou, Y.; Song, H.; Pang, K.; Song, H.; Minoofar, A. Turbulence-resilient pilot-assisted self-coherent free-space optical communications using automatic optoelectronic mixing of many modes. *Nat. Photonics* **2021**, *15*, 743−750.

(65) Richardson, D. J. Filling the light pipe. *Science* **2010**, *330*, 327−328.

(66) Sadatgol, M.; Özdemir, Ş. K.; Yang, L.; Güney, D. Ö. Plasmon injection to compensate and control losses in negative index metamaterials. *Phys. Rev. Lett.* **2015**, *115*, 035502.

(67) Ghoshroy, A.; Özdemir, Ş. K.; Güney, D. Ö. Loss compensation in metamaterials and plasmonics with virtual gain. *Opt. Mater. Express* **2020**, *10*, 1862−1880.

(68) Adams, W.; Sadatgol, M.; Güney, D. Ö. Review of near-field optics and superlenses for sub-diffraction-limited nano-imaging. *AIP Adv.* **2016**, *6* (10), 100701.

(69) Adams, W.; Sadatgol, M.; Zhang, X.; Güney, D. Ö. Bringing the 'perfect lens' into focus by near-perfect compensation of losses without gain media. *New J. Phys.* **2016**, *18*, 125004.

(70) Zhang, X.; Adams, W.; Sadatgol, M.; Guney, D. O. Enhancing the resolution of hyperlens by the compensation of losses without gain media. *Prog. Electromagn. Res. C* **2016**, *70*, 1.

(71) Zhang, X.; Adams, W.; Güney, D. Ö. Analytical description of inverse filter emulating the plasmon injection loss compensation scheme and implementation for ultrahigh-resolution hyperlens. *J. Opt. Soc. Am. B* **2017**, *34*, 1310−1318.

(72) Adams, W.; Ghoshroy, A.; Güney, D. Ö. Plasmonic superlens image reconstruction using intensity data and equivalence to structured light illumination for compensation of losses. *J. Opt. Soc. Am. B* **2017**, *34*, 2161−2168.

(73) Tuniz, A.; Kuhlmey, B. T. Subwavelength terahertz imaging via virtual superlensing in the radiating near field. *Nat. Commun.* **2023**, *14*, 6393.

(74) Ghoshroy, A.; Adams, W.; Zhang, X.; Güney, D. Ö. Active plasmon injection scheme for subdiffraction imaging with imperfect negative index flat lens. *J. Opt. Soc. Am. B* **2017**, *34*, 1478−1488.

(75) Ghoshroy, A.; Adams, W.; Zhang, X.; Güney, D. Ö. Enhanced superlens imaging with loss-compensating hyperbolic near-field spatial filter. *Opt. Lett.* **2018**, *43*, 1810−1813.

(76) Adams, W.; Ghoshroy, A.; Guney, D. O. Plasmonic superlens imaging enhanced by incoherent active convolved illumination. *ACS Photonics* **2018**, *5*, 1294−1302.

(77) Ghoshroy, A.; Adams, W.; Güney, D. Ö. Theory of coherent active convolved illumination for superresolution enhancement. *J. Opt. Soc. Am. B* **2020**, *37*, 2452−2463.

(78) Adams, W.; Ghoshroy, A.; Güney, D. Ö. Incoherent active convolved illumination enhances the signal-to-noise ratio for shot noise: Experimental evidence. *Phys. Rev. Appl.* **2022**, *18*, 064080.

(79) Ghoshroy, A.; Adams, W.; Güney, D. Ö. Super-resolution enhancement with active convolved illumination and correlations. *Active Photonic Platforms XI.*; SPIE, 2019, 67−75.

(80) Li, H.; Mekawy, A.; Krasnok, A.; Alù, A. Virtual parity-time symmetry. *Phys. Rev. Lett.* **2020**, *124*, 193901.

(81) Kim, S.; Peng, Y.-G.; Yves, S.; Alù, A. Loss compensation and superresolution in metamaterials with excitations at complex frequencies. *Phys. Rev. X* **2023**, *13*, 041024.

(82) Guan, F.; Guo, X.; Zeng, K.; Zhang, S.; Nie, Z.; Ma, S.; Dai, Q.; Pendry, J.; Zhang, X.; Zhang, S. Overcoming losses in superlenses with synthetic waves of complex frequency. *Science* **2023**, *381*, 766−771.

(83) Ghoshroy, A.; Adams, W.; Zhang, X.; Güney, D. Ö. Hyperbolic metamaterial as a tunable near-field spatial filter to implement active plasmon-injection loss compensation. *Phys. Rev. Appl.* **2018**, *10*, 024018.

(84) Chang, T. Y.; Hong, J. H.; Yeh, P. Spatial amplification: An image-processing technique using the selective amplification of spatial frequencies. *Opt. Lett.* **1990**, *15*, 743−745.

(85) Bos, J. P.; Roggemann, M. C. Technique for simulating anisoplanatic image formation over long horizontal paths. *Opt. Eng.* **2012**, *51*, 101704−101704.

(86) Li, R.; Luo, L.; Li, J.; Gao, X. Simulation of anisoplanatic imaging containing optical system parameters through atmospheric turbulence. *Optik* **2020**, *204*, 164177.

(87) Ren, Y.; Xie, G.; Huang, H.; Ahmed, N.; Yan, Y.; Li, L.; Bao, C.; Lavery, M. P.; Tur, M.; Neifeld, M. A. Adaptive-optics-based simultaneous pre-and post-turbulence compensation of multiple orbital-angular-momentum beams in a bidirectional free-space optical link. *Optica* **2014**, *1*, 376−382.

(88) Chen, J.; Kong, L.; Zhan, Q. Demonstration of a vectorial optical field generator with adaptive close loop control. *Rev. Sci. Instrum.* **2017**, *88*, 125111.

(89) Liu, J.; Wang, P.; Zhang, X.; He, Y.; Zhou, X.; Ye, H.; Li, Y.; Xu, S.; Chen, S.; Fan, D. Deep learning based atmospheric turbulence compensation for orbital angular momentum beam distortion and communication. *Opt. Express* **2019**, *27*, 16671−16688.

(90) Deledalle, C.-A.; Gilles, J. Blind atmospheric turbulence deconvolution. *IET Image Process.* **2020**, *14*, 3422−3432.

(91) Chen, G.; Gao, Z.; Wang, Q.; Luo, Q. Blind de-convolution of images degraded by atmospheric turbulence. *Appl. Soft Comput.* **2020**, *89*, 106131.

(92) Hua, X.; Pan, C.; Shi, Y.; Liu, J.; Hong, H. Removing atmospheric turbulence effects via geometric distortion and blur representation. *IEEE Trans. Geosci. Remote Sens.* **2020**, *60*, 1−13.

(93) Wang, N.; Zhu, L.; Ma, S.; Zhao, W.; Ge, X.; Gao, Z.; Yang, K.; Wang, S.; Yang, P. Deep learning-based prediction algorithm on atmospheric turbulence-induced wavefront for adaptive optics. *IEEE Photonics J.* **2022**, *14*, 1−10.

(94) Li, N.; Thapa, S.; Whyte, C.; Reed, A. W.; Jayasuriya, S.; Ye, J. Unsupervised non-rigid image distortion removal via grid deformation. *Proceedings/ IEEE International Conference on Computer Vision*; IEEE, 2021, 2522−2532

(95) Lau, C. P.; Lai, Y. H.; Lui, L. M. Restoration of atmospheric turbulence-distorted images via RPCA and quasiconformal maps. *Inverse Probl.* **2019**, *35*, 074002.

(96) Maulik, R.; San, O. A neural network approach for the blind deconvolution of turbulent flows. *J. Fluid Mech.* **2017**, *831*, 151−181.

(97) Singh, K.; Nape, I.; Buono, W. T.; Dudley, A.; Forbes, A. A robust basis for multi-bit optical communication with vectorial light. *Laser Photonics Rev.* **2023**, *17*, 2200844.

(98) Feng, B. Y.; Xie, M.; Metzler, C. A. TurbuGAN: An adversarial learning approach to spatially-varying multiframe blind deconvolution with applications to imaging through turbulence. *IEEE Trans. Inf. Theory* **2022**, *3*, 543−556.

(99) Durnin, J. Exact solutions for nondiffracting beams. I. The scalar theory. *J. Opt. Soc. Am. A* **1987**, *4*, 651−654.

(100) Shen, Y.; Pidishety, S.; Nape, I.; Dudley, A. Self-healing of structured light: A review. *J. Opt.* **2022**, *24*, 103001.

(101) Osborn, J.; Townson, M. J.; Farley, O. J.; Reeves, A.; Calvo, R. M. Adaptive Optics pre-compensated laser uplink to LEO and GEO. *Opt. Express* **2021**, *29*, 6113−6132.

(102) Shapiro, J. H. Reciprocity of the turbulent atmosphere. *J. Opt. Soc. Am.* **1971**, *61*, 492−495.

(103) Willner, A. E.; Ren, Y.; Xie, G.; Yan, Y.; Li, L.; Zhao, Z.; Wang, J.; Tur, M.; Molisch, A. F.; Ashrafi, S. Recent advances in high-capacity free-space optical and radio-frequency communications using orbital angular momentum multiplexing. *Philos. Trans. R. Soc., A* **2017**, *375*, 20150439.

(104) Zhang, L.; Shen, F.; Lan, B.; Tang, A. Mode-dependent crosstalk and detection probability of orbital angular momentum of optical vortex beam through atmospheric turbulence. *J. Opt.* **2020**, *22*, 075607.

(105) Banet, M. T.; Spencer, M. F. Compensated-beacon adaptive optics using least-squares phase reconstruction. *Opt. Express* **2020**, *28*, 36902−36914.

(106) Kim, J. J.; Fernandez, B.; Agrawal, B. Iterative wavefront reconstruction for strong turbulence using Shack−Hartmann wavefront sensor measurements. *J. Opt. Soc. Am. A* **2021**, *38*, 456−464.

(107) Guan, Z.; Zhao, C.; Yang, S.; Wang, Y.; Ke, J.; Zhang, H. Demonstration of a free-space optical communication system using a solar-pumped laser as signal transmitter. *Laser Phys. Lett.* **2017**, *14*, 055804.

(108) Castañeda, E. N.; Vázquez, J. C. G.; Alarcón, R. R.; Agha, I.; Zhan, Q.; Plick, W. N. Ince-Gauss beams in a turbulent atmosphere: The effect of structural parameters on beam resilience. *Opt. Continuum.* **2022**, *1*, 1777−1794.

(109) Zhan, Q. Cylindrical vector beams: From mathematical concepts to applications. *Adv. Opt. Photonics* **2009**, *1*, 1−57.

(110) Rosales-Guzmán, C.; Ndagano, B.; Forbes, A. A review of complex vector light fields and their applications. *J. Opt.* **2018**, *20*, 123001.

(111) Shen, Y.; Yang, X.; Naidoo, D.; Fu, X.; Forbes, A. Structured ray-wave vector vortex beams in multiple degrees of freedom from a laser. *Optica* **2020**, *7*, 820.

(112) Zhu, Z.; Janasik, M.; Fyffe, A.; Hay, D.; Zhou, Y.; Kantor, B.; Winder, T.; Boyd, R. W.; Leuchs, G.; Shi, Z. Compensation-free high-dimensional free-space optical communication using turbulence-resilient vector beams. *Nat. Commun.* **2021**, *12*, 1666.

(113) Zhao, Y.; Wang, J. High-base vector beam encoding/decoding for visible-light communications. *Opt. Lett.* **2015**, *40*, 4843.

(114) Cox, M. A.; Rosales-Guzmán, C.; Lavery, M. P.; Versfeld, D. J.; Forbes, A. On the resilience of scalar and vector vortex modes in turbulence. *Opt. Express* **2016**, *24*, 18105−18113.

(115) Gu, Y.; Korotkova, O.; Gbur, G. Scintillation of nonuniformly polarized beams in atmospheric turbulence. *Opt. Lett.* **2009**, *34*, 2261−2263.

(116) Ndagano, B.; Nape, I.; Cox, M. A.; Rosales-Guzman, C.; Forbes, A. Creation and detection of vector vortex modes for classical and quantum communication. *J. Light. Technol.* **2018**, *36*, 292.

(117) Efremidis, N. K.; Chen, Z.; Segev, M.; Christodoulides, D. N. Airy beams and accelerating waves: An overview of recent advances. *Optica* **2019**, *6*, 686−701.

(118) Zhou, H.; Su, X.; Duan, Y.; Song, H.; Zou, K.; Zhang, R.; Song, H.; Hu, N.; Tur, M.; Willner, A. E. Atmospheric turbulence strength distribution along a propagation path probed by longitudinally structured optical beams. *Nat. Commun.* **2023**, *14*, 4701.

(119) Korotkova, O.; Toselli, I. Non-classic atmospheric optical turbulence. *Appl. Sci.* **2021**, *11*, 8487.

(120) Chen, X.; Li, J.; Korotkova, O. Light scintillation in soft biological tissues. *Waves Random Complex* **2020**, *30*, 481−489.

(121) Wu, G.; Guo, H.; Yu, S.; Luo, B. Spreading and direction of Gaussian−Schell model beam through a non-Kolmogorov turbulence. *Opt. Lett.* **2010**, *35*, 715−717.

(122) Xu, Y.; Tian, H.; Dan, Y.; Feng, H.; Wang, S. Beam wander and M^2-factor of partially coherent electromagnetic hollow Gaussian beam propagating through non-Kolmogorov turbulence. *J. Mod. Opt.* **2017**, *64*, 844−854.

(123) Hao, X.; Allgeyer, E. S.; Lee, D.-R.; Antonello, J.; Watters, K.; Gerdes, J. A.; Schroeder, L. K.; Bottanelli, F.; Zhao, J.; Kidd, P. Three-dimensional adaptive optical nanoscopy for thick specimen imaging at sub-50*nm* resolution. *Nat. Methods* **2021**, *18*, 688−693.

(124) Booth, M.; Andrade, D.; Burke, D.; Patton, B.; Zurauskas, M. Aberrations and adaptive optics in super-resolution microscopy. *Microscopy* **2015**, *64*, 251−261.

(125) Ren, Y.; Li, L.; Wang, Z.; Kamali, S. M.; Arbabi, E.; Arbabi, A.; Zhao, Z.; Xie, G.; Cao, Y.; Ahmed, N.; et al. Orbital angular momentum-based space division multiplexing for high-capacity underwater optical communications. *Sci. Rep.* **2016**, *6*, 33306.

(126) Zhou, Y.; Gao, H.; Teng, J.; Luo, X.; Hong, M. Orbital angular momentum generation via a spiral phase microsphere. *Opt. Lett.* **2018**, *43*, 34−37.

(127) Cheng, L.; Hong, W.; Hao, Z.-C. Design and implementation of planar reflection spiral phase plate for beams with orbital angular momentum. *IET Microw. Antennas Propag.* **2017**, *11*, 260−264.

(128) Kong, F.; Zhang, C.; Bouchard, F.; Li, Z.; Brown, G. G.; Ko, D. H.; Hammond, T.; Arissian, L.; Boyd, R. W.; Karimi, E.; et al. Controlling the orbital angular momentum of high harmonic vortices. *Nat. Commun.* **2017**, *8*, 14970.

(129) Qiu, J.; Shen, B.; Zhang, X.; Bu, Z.; Yi, L.; Zhang, L.; Xu, Z. Vortex beam of tilted orbital angular momentum generated from grating. *Plasma Phys. Control. Fusion* **2019**, *61*, 105001.

(130) Lei, T.; Zhang, M.; Li, Y.; Jia, P.; Liu, G. N.; Xu, X.; Li, Z.; Min, C.; Lin, J.; Yu, C. Massive individual orbital angular momentum channels for multiplexing enabled by Dammann gratings. *Light: Sci. Appl.* **2015**, *4*, No. e257.

(131) Qin, F.; Wan, L.; Li, L.; Zhang, H.; Wei, G.; Gao, S. A transmission metasurface for generating OAM beams. *IEEE Antennas Wirel. Propag. Lett.* **2018**, *17*, 1793−1796.

(132) Bai, X.; Kong, F.; Sun, Y.; Wang, G.; Qian, J.; Li, X.; Cao, A.; He, C.; Liang, X.; Jin, R.; et al. High-efficiency transmissive

programmable metasurface for multimode OAM generation. *Adv. Opt. Mater.* **2020**, *8*, 2000570.

(133) Ahmed, H.; Kim, H.; Zhang, Y.; Intaravanne, Y.; Jang, J.; Rho, J.; Chen, S.; Chen, X. Optical metasurfaces for generating and manipulating optical vortex beams. *Nanophotonics* **2022**, *11*, 941−956.

(134) Wang, X.; Nie, Z.; Liang, Y.; Wang, J.; Li, T.; Jia, B. Recent advances on optical vortex generation. *Nanophotonics* **2018**, *7*, 1533−1556.

(135) Lian, Y.; Qi, X.; Wang, Y.; Bai, Z.; Wang, Y.; Lu, Z. OAM beam generation in space and its applications: A review. *Opt. Lasers Eng.* **2022**, *151*, 106923.

(136) Ke, X. *Generation, Transmission, Detection, and Application of Vortex Beams*; Springer Nature, 2023. DOI: .

(137) Wang, Y.; Landreman, P.; Schoen, D.; Okabe, K.; Marshall, A.; Celano, U.; Wong, H.-S. P.; Park, J.; Brongersma, M. L. Electrical tuning of phase-change antennas and metasurfaces. *Nat. Nanotechnol.* **2021**, *16*, 667−672.

(138) Abdollahramezani, S.; Hemmatyar, O.; Taghinejad, M.; Taghinejad, H.; Krasnok, A.; Eftekhar, A. A.; Teichrib, C.; Deshmukh, S.; El-Sayed, M. A.; Pop, E.; et al. Electrically driven reprogrammable phase-change metasurface reaching 80% efficiency. *Nat. Commun.* **2022**, *13*, 1696.

(139) Leitis, A.; Heßler, A.; Wahl, S.; Wuttig, M.; Taubner, T.; Tittl, A.; Altug, H. All-dielectric programmable Huygens' metasurfaces. *Adv. Funct. Mater.* **2020**, *30*, 1910259.

(140) Abdollahramezani, S.; Hemmatyar, O.; Taghinejad, M.; Taghinejad, H.; Kiarashinejad, Y.; Zandehshahvar, M.; Fan, T.; Deshmukh, S.; Eftekhar, A. A.; Cai, W. Dynamic hybrid metasurfaces. *Nano Lett.* **2021**, *21*, 1238−1245.

(141) Wang, R.; Wang, Y.; Jin, C.; Yin, X.; Wang, S.; Yang, C.; Cao, Z.; Mu, Q.; Gao, S.; Xuan, L. Demonstration of horizontal free-space laser communication with the effect of the bandwidth of adaptive optics system. *Opt. Commun.* **2019**, *431*, 167−173.

(142) Cheng, Z.; Li, C.; Khadria, A.; Zhang, Y.; Wang, L. V. High-gain and high-speed wavefront shaping through scattering media. *Nat. Photonics* **2023**, *17*, 299−305.

(143) Wei, X.; Shen, Y.; Jing, J. C.; Hemphill, A. S.; Yang, C.; Xu, S.; Yang, Z.; Wang, L. V. Real-time frequency-encoded spatiotemporal focusing through scattering media using a programmable 2D ultrafine optical frequency comb. *Sci. Adv.* **2020**, *6*, No. eaay1192.

(144) Wang, D.; Sahoo, S. K.; Zhu, X.; Adamo, G.; Dang, C. Non-invasive super-resolution imaging through dynamic scattering media. *Nat. Commun.* **2021**, *12*, 3150.

(145) Wang, N.; Zhu, L.; Yuan, Q.; Ge, X.; Gao, Z.; Wang, S.; Yang, P. Highly stable spatio-temporal prediction network of wavefront sensor slopes in adaptive optics. *Sensors* **2023**, *23*, 9260.

(146) Moazzam, A. A.; Ghoshroy, A.; Askari, R.; Güney, D. Ö. *Active convolved illumination towards enhanced remote sensing through a turbulent atmosphere*; AGU, 2023; p S11F0322.

(147) Cha, H.-S.; Lim, B.; Ko, Y.-C. Beam pointing optimization for spatial diversity MIMO free space optical communications. *Opt. Commun.* **2024**, *566*, 130693.

(148) Hu, Z.; Chen, Z.; Li, Y.; Benton, D. M.; Ali, A. A.; Patel, M.; Lavery, M. P.; Ellis, A. D. Adaptive transceiver design for high-capacity multi-modal free-space optical communications with commercial devices and atmospheric turbulence. *J. Light. Technol.* **2023**, *41*, 3397−3406.

(149) Zhang, N.; Xiong, B.; Zhang, X.; Yuan, X. High-capacity and multi-dimensional orbital angular momentum multiplexing holography. *Opt. Express* **2023**, *31*, 31884−31897.

(150) Hu, Z.; Li, Y.; Chen, Z.; Benton, D. M.; Ali, A. A.; Patel, M.; Lavery, M. P.; Ellis, A. D. Aiming for high-capacity multi-modal free-space optical transmission leveraging complete modal basis sets. *Opt. Commun.* **2023**, *541*, 129531.